Department of Physics and Astronomy
University of Heidelberg

Master Thesis in Physics
submitted by

Marius Sparn

born in Heidelberg (Germany)

2020

A Setup for Creating Arbitrary Potentials in a Two-dimensional ^{39}K BEC with a Digital Micromirror Device

This Master Thesis has been carried out by Marius Sparn at the
Kirchhoff-Institute for Physics in Heidelberg
under the supervision of
Prof. Dr. Markus K. Oberthaler

Abstract

A Setup for Creating Arbitrary Potentials in a Two-dimensional ^{39}K BEC with a Digital Micromirror Device

This thesis presents a setup capable of creating arbitrary potentials for a two-dimensional Bose-Einstein condensate. A Digital Micromirror Device is used to spatially modulate and thus shape a laser beam. Reimaged to the position of the atomic cloud, this laser beam can create spatially configurable potentials. Numerical calculations of the resulting potentials and light intensities in the trapping region are carried out for ^{39}K and a laser with a wavelength of $532\,\mathrm{nm}$. Special emphasis is given to the implementation of variable intensities (grayscales) via spatial averaging and mitigation of diffraction effects. It is shown that a high resolution of the DMD is crucial for maximum grayscales and mitigation of distortions. Results from a test setup are presented along with two algorithms aiming at the minimization of distortions and diffraction effects. This setup can be transferred to the main experiment with only small modifications.

Zusammenfassung

Ein Aufbau zur Erzeugung beliebiger Potentiale in einem zweidimensionalen ^{39}K BEC mit einem Digital Micromirror Device

In dieser Arbeit wird ein Aufbau vorgestellt, der in der Lage ist, beliebige Potentiale für ein zweidimensionales Bose-Einstein-Kondensat zu erzeugen. Ein Digital Micromirror Device wird verwendet, um einen Laserstrahl räumlich zu modulieren und somit zu formen. Auf die Position der Atomwolke abgebildet, kann dieser Laserstrahl räumlich konfigurierbare Potentiale erzeugen.
Numerische Berechnungen der resultierenden Potentiale und Lichtintensitäten im Fallenbereich werden für ^{39}K und einen Laser mit einer Wellenlänge von $532\,\mathrm{nm}$ durchgeführt. Besonderer Wert wird auf die Implementierung variabler Intensitäten (Graustufen) durch räumliche Mittelung und die Minimierung von Beugungseffekten gelegt. Es wird gezeigt, dass eine hohe Auflösung des DMD entscheidend für maximale Graustufen und die Verringerung von Beugungseffekten ist.
Die Ergebnisse einer Versuchsanordnung werden neben zwei Algorithmen vorgestellt, die auf die Minimierung von Verzerrungen und Beugungseffekten ausgelegt sind. Dieser Aufbau kann mit geringfügigen Modifikationen in das Hauptexperiment übernommen werden.

Contents

List of Figures

1 Introduction

At the beginning of the 20th century, the classical description of physical phenomena progressively turned out to fail when approaching the atomic scale. Reconciling the dual nature of matter as particle or wave or the observation of the quantization of energy states opened up a whole new field in physics, named Quantum Mechanics. However, it took about half a century until a tremendous boost for the experimental exploration of quantum mechanical phenomena set in by the invention of powerful coherent light sources (LASER) in 1960. Applying coherent light at high-density power over a wide range of frequency is an ideal tool to address physical phenomena on an atomic scale.

In 1970 Arthur Ashkin, at Bell Laboratories, intended to use the radiation pressure of a laser beam to exert a force on micron-sized particles [1]. In his experiment, he suspended latex spheres in water, shed laser light through the water, and watched the movement of the latex spheres. Initially, he expected these forces on the spheres to be in beam direction only [2]. However, the particles accumulated in the center of the beam and even stayed there when he started moving the beam. The spheres obviously were attracted to the area of high intensity in the center of the beam. This observation formed the basis for the invention of optical tweezers or, more generally speaking and in the context of neutral atoms, for the invention of the electrical dipole trap, where the application of two crossing laser beams each of them focused to the intersecting area confines atoms in all spatial dimensions. However, to achieve these trapping conditions, radiation pressure exerted on the atoms must be avoided by choosing the laser frequency smaller than the transition frequencies of the atomic absorption levels (red detuning). In case of blue detuning, the atoms experience a repelling force.

The enormous potential of these inventions for the exploration of matter on the atomic scale was demonstrated impressively in 1995 by the groups of Cornell and Wieman at JILA [3] and Ketterle at MIT [4] who achieved to produce a coherent state of bosonic particles in a dilute gas. This experimental success opened up a whole new subfield in experimental physics dedicated to explore in detail the properties of such a Bose-Einstein Condensates (BEC), predicted by Bose and Einstein in their studies about the low-energy state of identical particles with integer spin about 70 years earlier [5, 6].

The intriguing feature of this state of matter is that the BEC can be described by a single condensate wavefunction, where below the critical temperature, most of the particles will occupy the lowest quantum state of the ensemble. This allows for the investigation of a macroscopic system, completely governed by the laws of quantum mechanics. While those first Bose-Einstein Condensates (BEC), were obtained in magnetic traps, it can be of advantage to produce them in (or transfer them to) an optical dipole trap. Besides the fact that magnetic traps only trap atoms with specific magnetic hyperfine substates, in a dipole trap, the magnetic field can then additionally be used to tune the interaction strength in the BEC, via Feshbach-resonances [7]. This allows the realization of a variety of different dynamical regimes to study.

The particular motivation for this work is an experiment, which aims to produce two-dimensional BECs of ^{39}K (BECK) with tunable interactions. Confinement in gravity direction is implemented with a dipole trap, realized by a lattice structure produced with a blue detuned laser. Additional potential walls are needed to set the boundaries for the resulting two-dimensional geometry. This thesis describes the design, building and testing of a setup, which provides the capabilities to produce these potential wall structures. A blue detuned laser beam is modulated by a commercially available Digital Micromirror Device (DMD), usually applied in beamers for PC- or entertainment applications, to achieve structured light patterns. By reimaging the resulting pattern into the atom plane inside the trap, defined by the lattice, arbitrary wall shapes can be produced. Moreover, setup and programming are open to cope with future demands by allowing for shaping arbitrary potential landscapes. This is done with additional implementation of a controlled variation of the intensity of the light reflected at the DMD (concept of grayscales).

Outline

First, theoretical background knowledge is presented to motivate and explain the experimental setup and the choice of its components (Chapter2). The most important selection criteria include the requirements for the DMD-chip, the total laser intensities needed to create a trap wall structure with sufficiently large trap potential (which is probed by a numerical calculation of the resulting potential), the capability to vary the intensity of the trap structure on a small scale (a second numerical calculation gives insight in the implementation of grayscales in this setup) which is related to the last criterion of the mitigation of diffraction effects, resulting from the diffraction-limited reimaging of the walls. These are given in Chapter 3. In Chapter 4, a test setup is presented, and results are discussed. This setup differs only slightly from the planned configuration and can, in large parts, be transferred to the experiment. Chapter 5 presents two different algorithms, designed to measure and compensate distortions in the resulting trap potential patterns. Although the second algorithm is in an early stage of development, it could prove itself essential for the mitigation of diffraction effects.

2 Theoretical and Experimental Background

2.1 Dipole Potentials for Alkali Atoms

The reason for the attraction of the latex spheres to the high power regions in Ahskin's experiment can be understood in terms of different refractive indices of the spheres and the surrounding water. This leads to the refraction of incoming light rays, in this case, towards the center of the sphere. As the outgoing light has experienced a force towards the center, the sphere itself experienced a force in the opposite direction. For an asymmetric incoming intensity distribution, the sphere, therefore, experiences a net force towards the high-intensity center of the beam. In the case of a focused beam, the resulting force points towards the focus. This leads to a stable position behind the focus, where it cancels out the radiation pressure of absorbed photons in the beam direction. The concept of exerting forces on particles with laser light can also be employed to trap atoms. While the refraction picture is not sufficient to describe the phenomenon in this case, the underlying principle remains the same. The dipole forces can be understood in a two-level model of an atom. To describe this model, many textbooks employ an oscillator with complex polarizability, driven by the electric field of the light. This is similar to the refractive index, as a consequence of the materials electric susceptibility.

To get a description for the multi-level alkali atoms however, this section presents a treatment in a dressed state picture, which is based on [8], where the dipole potential is identified with the AC-Stark shift. The multi-level treatment will also show, that at large detunings a two-level description can be sufficient, which will be shown first. The AC-Stark shift can be calculated in second-order perturbation theory. For the eigenenergies $\mathcal{E}_i$ and the eigenstates $|i\rangle$ of the atom this results in:

$$\Delta E_i = \sum_{j \neq i} \frac{|\langle j| \left(-\hat{\mu}\vec{E}\right) |i\rangle|^2}{\mathcal{E}_i - \mathcal{E}_j} \tag{2.1}$$

with the dipole operator $\hat{\mu}$ and field $\vec{E}$, and the sum running over all eigenstates $|j\rangle$, unequal $|i\rangle$. Note that the relevant eigenenergies are the eigenenergies of the isolated atom plus the photon field, while the interaction Hamiltonian is considered to be the perturbation.

Two-level Atom

When the groundstate energy of the isolated two-level atom is set to zero, the energy $\mathcal{E}_g = n\hbar\omega$ is, therefore, that of the photon field and $\mathcal{E}_e = (n-1)\hbar\omega + \hbar\omega_0 = -\hbar\Delta_{eg} + n\hbar\omega$ (with ω_0, being the resonance angular frequency of the transition). This results in:

$$\Delta E_{g/e} = \pm\frac{|\langle e|\,\mu\,|g\rangle\,|^2}{\Delta}|E|^2 \tag{2.2}$$

where the signs correspond to the energy shift of the ground state $|g\rangle$ (+) and excited state $|e\rangle$ (-). To get rid of the dipole matrix element one can substitute with the decay rate:

$$\Gamma = \frac{\omega_0^3}{3\pi\epsilon_0\hbar c^3}|\langle e|\,\mu\,|g\rangle\,|^2 \tag{2.3}$$

which (with the intensity $I = 2\epsilon_0 c|E|^2$) brings eq. 2.2 into the form:

$$U_{dip} = \frac{3\pi c^2}{2\omega_0^3}\frac{\Gamma}{\Delta}I \tag{2.4}$$

Because the detuning Δ in the trap is large, the occupation of the excited state is negligible. In that case the energy shift of the ground state can be considered to be the relevant dipole potential, which has been done here. For negative detuning (red detuned), U_{dip} lowers the potential, and the corresponding force points towards higher intensities, whereas for blue detuning the opposite is the case.

To get an expression for the scattering rate Γ_{sc}, one can interpret photon scattering as subsequent processes of absorption and emission. Together with the symmetry of the dipole matrix element this leads to:

$$\hbar\Gamma_{sc} = \frac{3\pi c^2}{2\hbar\omega_0^3}\left(\frac{\Gamma}{\Delta}\right)^2 I \tag{2.5}$$

While the potential is proportional to I/Δ, the scattering rate is proportional to I/Δ^2. This means for proportionally increasing the laser intensity and the detuning, one gets the same potential, while heating due to scattering decreases. Depending on the geometry, blue detuned traps can also be of advantage, since the atoms tend to reside at low intensities.

Multi-level (Alkali-)Atom

In case of a multi level atom with multiple ground- and/or excited states, one has to know their relative line strengths (and obviously energies). The corresponding Clebsch-Gordon coefficients c_{ij} then allow to calculate the state dependent potential for the ground states $|g_i\rangle$:

$$U_{dip,i} = \frac{3\pi c^2\Gamma}{2\omega_0^3}I\sum_j\frac{c_{ij}^2}{\Delta_{ij}} \tag{2.6}$$

Fortunately, in the case of detunings much larger than the hyperfine splitting of the excited states ($\Delta \ll \Delta_{hfs,e}$), the c_{ij} can be replaced by their sum, which is equivalent to the picture of unresolved hyperfine splitting (typically the case for ^{39}K, see Fig.2.1). For alkali atoms in

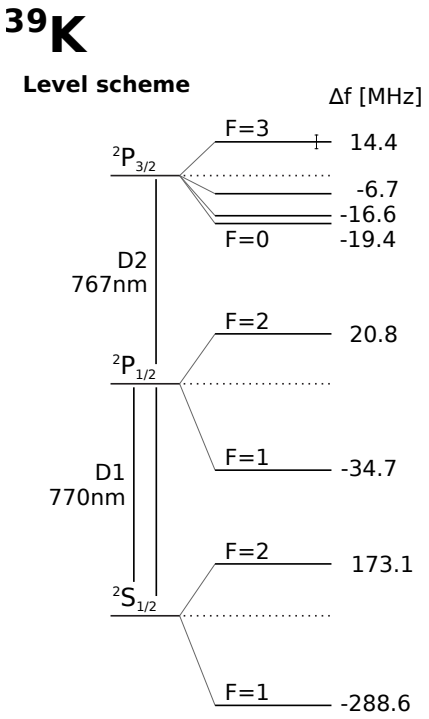

Figure 2.1 Level Structure of $^{3}9$K. Note that due to orders of magnitude in between the respective energy scales, hyperfine and fine splitting as well as the overall transition are not to scale. Image courtesy of Celia Viermann (BECK Team) with values taken from [9]

general with their characteristic D-line doublett ($^2S_{1/2} \rightarrow^2 P_{1/2},^2 P_{3/2}$) eq.2.6 then takes the form:

$$U_{dip,F} = \frac{\pi c^2 \Gamma}{2\omega_0^3} \left(\frac{2 + \mathcal{P} g_F m_F}{\Delta_{2,F}} \frac{1 - \mathcal{P} g_F m_F}{\Delta_{1,F}} \right) \tag{2.7}$$

where the F denote the hyperfine state of the ground state and 2 and 1 the line centers of the excited states. $\mathcal{P} = 0, \pm 1$ is the polarization of the laser m_F the magnetic substate and g_F the lande factor. Similar to eq. 2.5 the scattering rate can again be determined:

$$\Gamma_{sc} = \frac{\pi c^2 \Gamma^2}{2\hbar\omega_0^3} \left(\frac{2}{\Delta_{2,F}^2} + \frac{1}{\Delta_{1,F}^2} \right) I \tag{2.8}$$

For large detunings the difference between the two Δ is small and the hyperfine splitting of the ground state becomes negligible. In that case the influence of polarization is also small. Typically linear polarization is chosen, which has the additional advantage, that all magnetic sublevels are shifted equally. In the extreme case of very large detuning, the fine structure splitting is small in comparison and the system can again be described by eq. 2.4.

Introducing a spatial modulation of the intensity, results in the same modulation of the potential. This allows for potential shaping by modulating a laser beam with a Digital Micromirror Device.

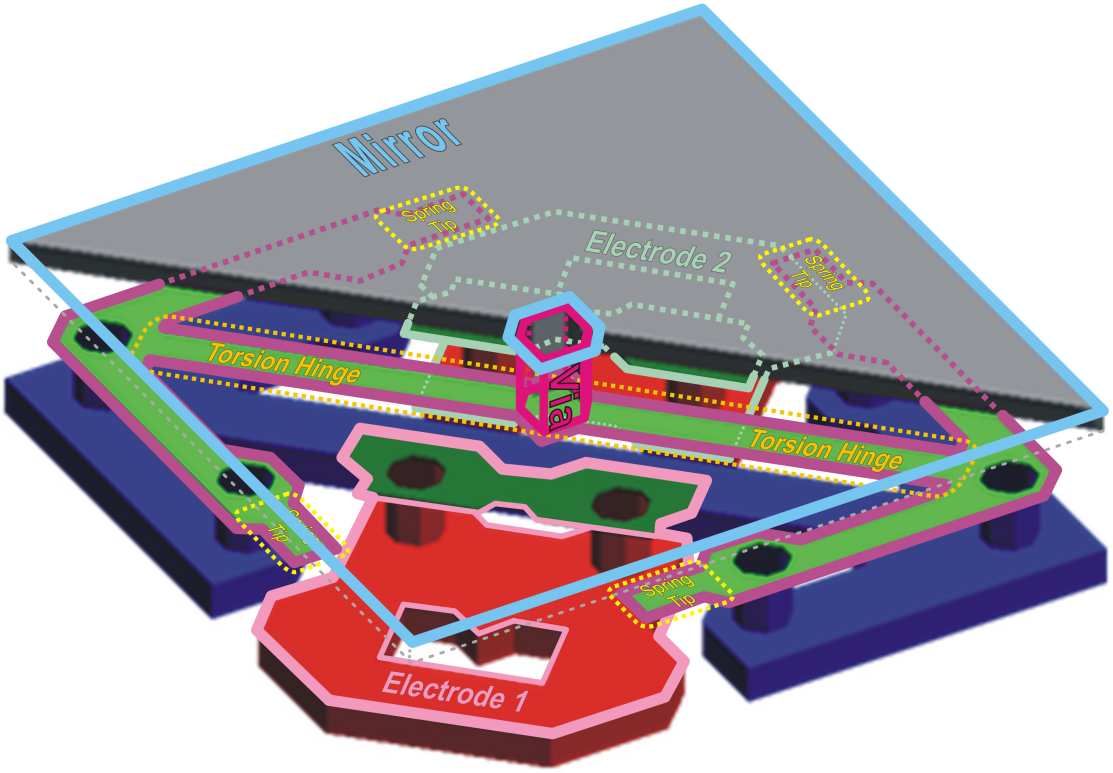

Figure 2.2 Illustration of a single aluminum mirror on the DMD. Individual mirrors can be flipped, via the electrostatic force of two electrodes. Spring tips define the stable positions of the ON- and OFF-state at $\pm 12°$. Image property of Texas Instruments [12]

2.2 DMD Working Principle

A Digital Micromirror Device (DMD) is a special kind of a Spatial Light Modulator (SLM). SLMs in general, are dynamically adaptable amplitude masks, capable of producing almost arbitrary light patterns. In contrast to the most widespread SLM technology, the Liquid Crystal one like in LCDs, a DMD can only be used as a reflective amplitude mask as it consists of an array of micrometer scale mirrors. These aluminium mirrors are mechanically flipped to reflect light. While nowadays DMDs are widely used commercially for example in video projectors, head-up displays in cars, 3D-scanners and printers or for lithography in the semiconductor industry, they also have a wide range of scientific applications. Besides potential shaping for ultra-cold-atom experiments, they are for example used for wavefront correction, beamshaping[10] and dynamically controlled optical tweezers [11].

To achieve the individual control of single mirrors, these are mounted on a torsion hinge (see Fig. 2.2). A torque is applied via the electrostatic force of two electrodes. Spring tips on either side define the stable positions of $\pm 12°$. While in operation all the mirrors are in either one of these ON-/OFF-positions. To change a mirrors position, first the new state has to be loaded in an underlying CMOS-cell. During a subsequent mirror clocking pulse a whole block of mirrors is then released and re-landed according to the saved states [12].

As can be seen in Fig. 2.2 the mirrors are hinged along their diagonal axis. This means their axis of rotation is oriented at $45°$ with respect to the rows and columns on the chip. To have

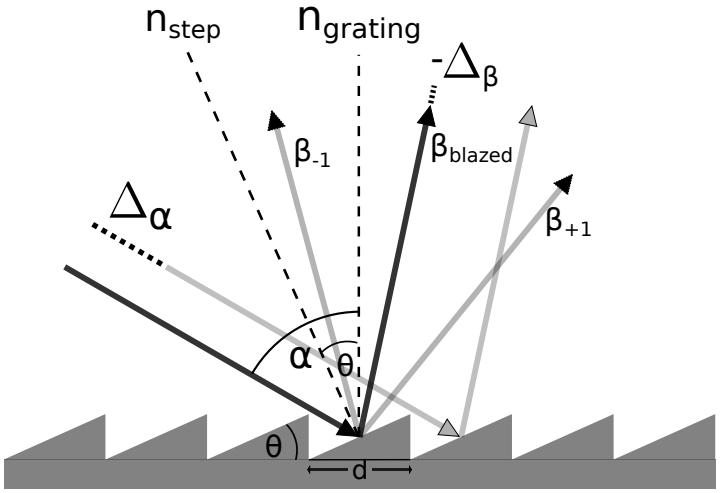

Figure 2.3 Illustration of a blazed grating with periodicity $1/d$ illuminated under angle α. Outgoing diffraction orders are denoted with angles β_i and arise whenever the resulting path difference $\Delta_\alpha + \Delta_\beta$ is a multiple of the wavelength. If the blazed condition is satisfied, one of those orders overlaps with the maximum of the single steps, resulting in maximum diffracted power in that order. Like a mirror, the maximum of the single step is at equal input and output angles, relative to the normal vector n_{step}, which differs by the tilt θ from that of the grating $n_{grating}$.

the resulting light paths of the ON- and OFF-position as well as the illumination parallel to the optical table, the DMD therefore has to be mounted at $45°$. For naively treating the DMD like a mirror, illumination under $24°$ then results in the output of the ON-state being normal to the plane of the chip. However, in applications with coherent light the blazed grating nature of the chip has to be taken into account (see 2.3 and 4.1).

2.3 Blazed Grating

Because the individual mirrors of the DMD are on the micrometer scale and arranged in a periodic structure on the chip, it acts as diffraction grating for the incoming light. Therefore multiple diffraction orders arise, which have different intensities, due to the extensiveness of the mirrors. In the following the conditions to be satisfied for maximum power in a specific order are derived by ray optics. If those are met, the DMD acts as a blazed grating.

A blazed grating is a diffraction grating with maximized grating efficiency for a given wavelength and diffraction order. It consists of steps, that are tilted at an angle θ relative to the gratings normal vector (see Fig. 2.3).

One could treat a grating with periodicity d^{-1} in the framework of Fourier optics (presented subsequently). For $\theta = 0$ and light incident under normal angle, the grating can be modeled as a convolution of delta-functions with periodicity of the grating and a box function. The resulting far field is proportional to the Fourier transform (see eq. 2.18 in the next section). Therefore it will consist of the diffraction pattern of the grating multiplied with the transformed box function as an envelope. (The angle of illumination α and the tilt θ can be included in the form of the corresponding phase factors over the step and grating function.)

However, in the application of a DMD the influence of α and θ, in particular on the relative shift between grating and envelope, is the relevant factor. Therefore the resulting outgoing angles of maximal intensity β will be inferred from path differences $\Delta = \Delta_\alpha + \Delta_\beta$ and their resulting phase shifts (see Fig. 2.18). For that parallel rays are considered to interfere at $z \to \infty$. The step will not be discussed in detail, since it has only one configuration for which all phase differences cancel out over the whole area. Like a mirror, this is the case for the outgoing angle β' being the inverse angle of incidence α'. Relative to the normal vector of the grating this reads:

$$\beta = -\alpha + 2\theta \tag{2.9}$$

The more interesting case arises for the periodic structure of the grating. Whenever Δ between two neighbouring mirrors is a multiple of the wavelength λ, this is true for all of them. Therefore multiple maxima have the same amplitude for β_i fulfilling the condition:

$$\Delta = m\lambda = d(\sin(\alpha) + \sin(\beta_i)) \tag{2.10}$$

with $m \in \mathbb{Z}$. For combinations of angles α, β and θ that meet both conditions from 2.9 and 2.10, the maximum of the envelope and the grating overlap. This leads to maximum diffraction efficiency. A simple way to meet the first condition 2.9 is to set all three angles equal. In this so called Littrow configuration the choice of m still leaves options open for a given wavelength. For the DMD however, d as well as θ are fixed and an output angle of $\beta = 0°$ is desired. For these conditions the blaze condition can not be met for arbitrary wavelengths. More on this can be found in 4.1, where the illumination is discussed in detail.

2.4 Fourier Optics

The output optics, that reimage the DMD patterns into the atom plane, have a major influence on the potential shapes that can be produced, the ability to mitigate diffraction orders at walls, and the grayscales available for potential shaping, since its resolution is diffraction-limited. In this section a mathematical description will be derived in the framework of Fourier optics, that allows for calculation of the resulting light intensities in the atom plane.

To describe the phenomena responsible for this alteration of shape (and overall intensity), the wave nature of light needs to be considered. This wave nature can be directly derived from the Maxwell equations (e.g. [13], that this summary is based on) leading to the wave equation in vacuum:

$$\nabla^2 U - \frac{1}{c^2}\frac{\partial^2 U}{\partial t^2} = 0 \tag{2.11}$$

with the complex wavefunction $U(\vec{r}, t)$ being solutions of the form:

$$U(\vec{r}, t) = A(\vec{r}) \exp(i\Phi(\vec{r})) \exp(i\omega t) \tag{2.12}$$

where $A(\vec{r})$ is the real amplitude and $\Phi(\vec{r})$ the position dependent phase factor. Restriction to a single frequency ω is made, which will be kept throughout this section. However, since superpositions of these solutions are still valid solutions of the wave equation, this is merely a

choice of basis. It is a convenient one, as it allows to write 2.11 in a time independent form (with $k = \omega/c$), that is called Helmholtz equation:

$$\nabla^2 U(\vec{r}) + k^2 U(\vec{r}) = 0 \tag{2.13}$$

the complex amplitude $U(\vec{r})$ is directly related to the resulting intensity:

$$I = |U(\vec{r})|^2 \tag{2.14}$$

One solution to the Helmholtz equation is the plane wave:

$$U_{plane}(x, y, z) = A \exp(i(k_x x + k_y y + k_z z)) \tag{2.15}$$

where the amplitude A is now in general complex, allowing for an offset phase. The wavenumbers k_i are related over their quadratic sum, which is determined by the wavelength:

$$\vec{k}^2 = k_x^2 + k_y^2 + k_z^2 = (2\pi/\lambda)^2 \Leftrightarrow k_z = \sqrt{(2\pi/\lambda)^2 - (k_x^2 + k_y^2)} \tag{2.16}$$

Since sums of those waves are still valid solutions, this allows for decomposition of arbitrary waves into a superposition of plane waves with different wavevectors $\vec{k}$. This is the foundation of describing the propagation of light in the framework of Fourier optics.

Starting from an arbitrary distribution $f(x, y)$ in the optics input plane, the decomposition is related via the Fourier Transform:

$$f(x, y) = \int_{-\infty}^{\infty} \int_{-\infty}^{\infty} F(k_x, k_y) \exp(i(k_x x + k_y y)) dk_x dk_y \tag{2.17}$$

where one can identify the amplitude A in 2.15 with one frequency (or wave vector) combination of the distribution $F(k_x, k_y)$. Recalling that two spatial frequency components determine the third one (eq. 2.16), this defines the superposition of plane waves at $z = 0$. While the optical axis z is the normal vector of the input plane, each of the plane waves will propagate in its k-direction, which is under angles $\theta_x \approx k_x/k$ and $\theta_y \approx k_y/k$ to z. This approximation is only valid for small angles and in this context called the paraxial approximation.

In this framework it is intuitive to see, that for sufficiently large distances $z = d$ (far field), the different contributing plane waves will decompose in the (x, y)-plane, due to their different $\vec{k}$. At every point (x, y) only the wave component which fulfils $k_x = xk/d$ and $k_y = yk/d$ contributes. All other components interfere destructively and the resulting output $g(x, y)$ directly depends on the amplitude in the frequency domain $F(k_x, k_y)$:

$$g(x, y) = h_0 F\left(\frac{xk}{d}, \frac{yk}{d}\right) \tag{2.18}$$

the complex prefactor $h_0 = \frac{i}{\lambda d} \exp(-ikd)$ accounts for the spread (or mathematically the rescaled coordinates in Fourier space) and the accumulated phase. Note that this is only valid for large distances d such that the phase only depends on d, but not on x and y (Fraunhofer approximation). This is the case, whenever the second order of the expansion of the phase factor:

$$kd\sqrt{1 - \theta^2} = kd\left(1 - \theta^2/2 + \theta^4/8...\right), \tag{2.19}$$

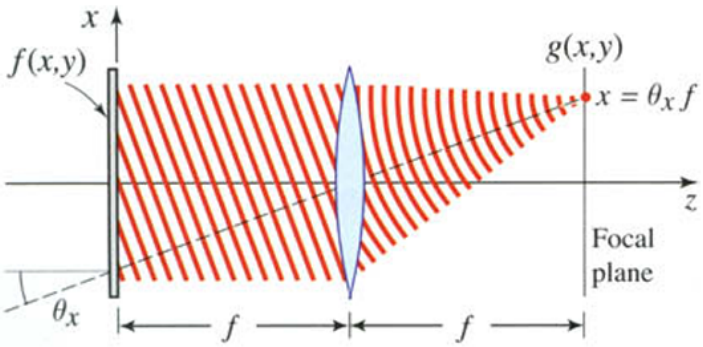

Figure 2.4 Illustration of the optical Fourier transform with a lens. The spatial frequency component that results in a plane wave with angle θ_x is focused to $x = \theta_x f$. In this process the lens transforms the plane wave into a paraboloidal wave. A description of this can be found in [13], where also this image is taken from.

where θ denotes the angle to the optical axis, is small (comp. 2.16). Sometimes Fresnel numbers $N_F = a^2/\lambda d \ll 1$ are stated, where a^2 is the area contributing to the input or output planes, justifying the cut-off in the expansion.

Instead of free space propagation over large distances, a lens can be used, which shifts the Fourier-pattern from $d \to \infty$ into its focus f. In the area of validity of the Fresnel approximation, which in turn takes the expansion up to second order into account, this can be calculated. While the less restrictive condition $N_F\theta^2/4 \ll 1$ applies, the phase depends on the (x, y)-position:

$$g(x,y) = h_l \exp\left(ik\frac{(x^2+y^2)(d-f)}{2f^2}\right) F\left(\frac{xk}{f}, \frac{yk}{f}\right) \tag{2.20}$$

here d is the position of the lens and $h_l = i/(\lambda f)\exp(-ik(d+f))$. The lens Fourier-transforms an incoming field distribution $f(x, y)$ into its focal plane. If the initial distribution is placed at its other focal plane, the phase factor over the (x,y)-plane vanishes in addition. With this, one can construct a representative optical imaging system that describes the influence of the output optics.

2.4.1 Resolution, Numerical Aperture and the 4f-Imaging System

The spatial resolution of an optical system is directly tied to the spatial frequency components (e.g in terms of k_x and k_y) it is able to image. Even without any optics the system is therefore inherently limited by the used wavelength. In 2.17 it was shown how a field distribution $f(x, y)$ can be constructed from plane waves. For this construction to be exact, the whole Fourier space needs to be included (therefore the integrals run from $-\infty$ to ∞). Following eq. 2.16 spatial frequency components for which $k_x^2 + k_y^2 > (2\pi/\lambda)^2$ lead to complex k_z. Insertion in 2.15 shows, that those result in exponential decay instead of propagation of the wave. Therefore

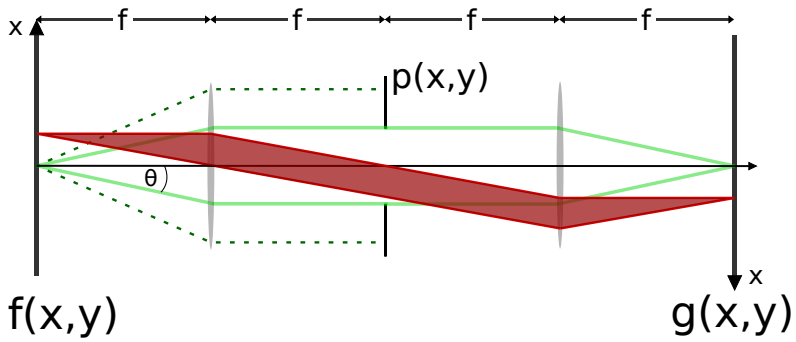

Figure 2.5 4f-imaging system consisting of two lenses with focal length f and an aperture $p(x, y)$ in the Fourier plane in between. The aperture restricts the NA $\propto \theta$ (illustrated in green), although the lens still transforms higher spatial frequencies (dotted line). $g(x, y)$ is a real image of the input $f(x, y)$ with flipped coordinates (ray-traced path in red).

these frequency components will not be available for reconstruction of $f(x, y)$ in the far field, regardless of the imaging system used. Any optical components employed subsequently, may only further restrict the spatial frequencies that are able to propagate through the setup.

As a measure of this, the numerical aperture (NA) of an optical element or an imaging system is a dimensionless number defined as:

$$\text{NA} = n \sin(\theta) \tag{2.21}$$

where n is the refractive index of the propagating medium and θ is the highest half angle under which the light can enter (and propagate through) the optics. In ray optics a ray at this angle is also called marginal ray. In the framework of plane waves this angle spans the cone of maximal spatial frequencies:

$$\sin(\theta) = (k_x^2 + k_y^2)^{1/2} \lambda / 2\pi \tag{2.22}$$

For the ability to reconstruct the the initial field distribution, it makes no difference where those frequencies are lost. In the following therefore a 4f-setup (fig. 2.5), as a representative optical imaging system, will be analyzed. It consists of two ideal lenses and an aperture, representing all those losses of frequencies discussed before. The initial field distribution $f(x, y)$ is positioned in the front-focus of the first lens. Following eq. 2.20 this results in the Fourier transformed distribution $F(k_x, k_y)$ in its focus at $z = 2f$ (with the additional phase factor over the plane vanishing). There the aperture is placed, which has a transmission $p(x, y)$ of 1 inside its radius a and 0 outside:

$$p(x, y) = \begin{cases} 1 & x^2 + y^2 < a^2 \\ 0 & else \end{cases} \tag{2.23}$$

The second lens is used for back-transformation with coinciding foci. At position $z = 4f$ (hence the name) the output $g(x, y)$ can be calculated by subsequently applying 2.20, 2.23 and again the lens equation to $f(x, y)$:

$$\begin{aligned} g(x, y) &= h_l \mathcal{F} \left(h_l \mathcal{F}[f(x, y)] p(x, y) \right) \\ &= h_l^2 f(x, y) * \mathcal{F}(p(x, y)) \end{aligned} \tag{2.24}$$

For the second line, linearity as well as the convolution theorem for the Fourier transformation was used. To get the field distribution in the output plane ($atz = 4f$), the initial field distribution has to be convoluted with the Fourier transform of the aperture. This setup can in principle be used for all kinds of manipulations on the Fourier components of the original distribution. If different focal lengths are employed an additional magnification can be achieved (see 2.20 and resulting rescaling in the Fourier plane). The fact that no residual phase factors in the (x,y)-plane remain after the back transformation, is an additional advantage of this specific setup. For example a collimated beam in the input plane is again collimated in the output plane. For the circular aperture used here, the Fourier transform can be represented with the order-1 Bessel function of the first kind $J_1(x)$:

$$\mathcal{F}(p(x,y)) = \frac{2J_1(kra/f)}{kra/f} \tag{2.25}$$

where r is the distance from the center in the output plane. This function has its first zero at $kr_0a/f = 1.22\pi$ (see Fig. 2.6).

As a measure of the resolution one typically looks at the way a single point is transformed by the optical setup. The so called Point Spread Function (PSF) is the intensity of a single point in the output plane. For $f(x,y) = \delta(0,0)$ the convolution in eq 2.24 is redundant and the result is proportional to 2.25. Squaring to get the intensity, leads to the Airy disc, the PSF of a circular aperture. In analogy the non-squared field distribution will in the following be called field-PSF. (Eq. 2.25 is sometimes referred to as Airy function. Because this term is ambiguous, it will not be used in the following.)

The Rayleigh criterion states that two points are resolvable, if their PSFs overlap at most to the point, where their maxima coincide with the first minimum of the other. The minimal resolvable distance d_{min} is therefore the position of the first zero r_0. Identifying a/f with $\sin(\theta)$ (and reinserting n which was taken to be 1 here) leads to the Rayleigh criterion in its known form:

$$d_{min} = \frac{1.22\lambda}{2\mathrm{NA}} \tag{2.26}$$

The minimal resolvable distance is inversely proportional to the opening angle of the optical system, or, in other words, to the maximum spatial frequencies, which are available for the reconstruction of the initial distribution.

2.5 Experimental Context

In the BECK-experiment a Bose-Einstein-Condensate (BEC) of ^{39}K is produced. Feshbach resonances are employed to tune the interactions in the condensate and during the process of condensation. The long-term goal is to load it into a tunable 2D-trap geometry, which then allows for a large range of Hamiltonians and initial conditions to be realized. This section gives a short overview of the cooling process to reach the condensate phase. Besides that, special emphasis is placed on the planned optical dipole trap setup, whose capabilities shall be enhanced by the use of a DMD. Also the imaging setup will be discussed in parts, because the optical system of the DMD overlaps with it.

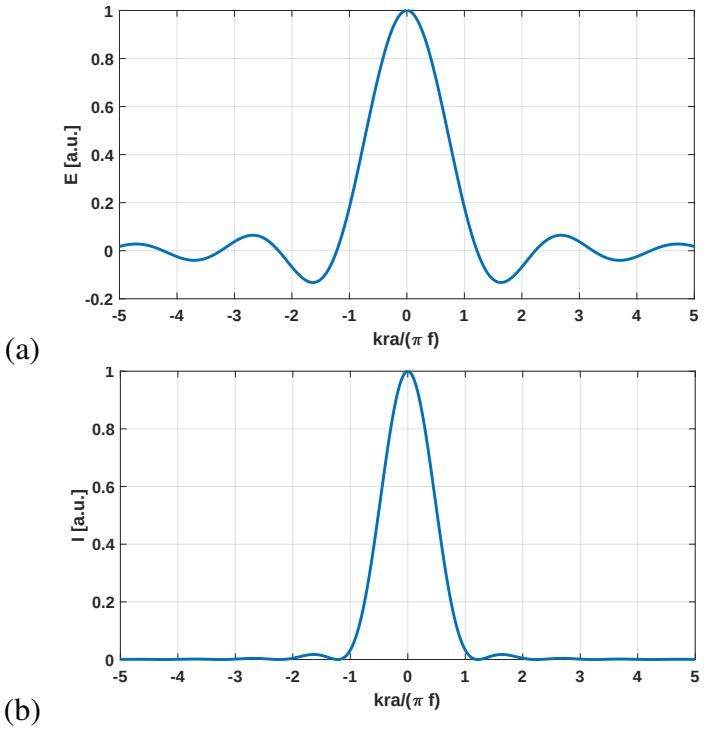

(a)

(b)

Figure 2.6 Fourier transform of a round aperture, the field-PSF (a) and resulting intensity, the PSF (b). Both functions have their first zero at $kra/(\pi f) = 1.22$, which corresponds to the resolution limit in the Rayleigh criterion.

Production of the BEC

To get thermal atoms of ^{39}K to the point where they form a condensate, various cooling techniques have to be applied successively, spanning nine orders of magnitude in temperature. From the thermal background produced by an oven, atoms are pre-cooled in a Magneto-Optical-Trap (MOT) [14] . It confines in two dimensions only, which is why the resulting atom cloud has a line shape. An additional push beam that is aligned with it transfers the pre-cooled atoms through a differential pumping stage into the science chamber. It has a much lower background pressure, which is crucial for the lifetime of the BEC. There a 3D-MOT confines the atoms in all spatial dimensions and cools the atoms further. For MOTs in general, the temperatures that can be achieved are limited by the Doppler temperature, which is about $145\,\mu$K for ^{39}K [9].

Employing sub-Doppler cooling techniques can be challenging for this species, since it has a small hyperfine splitting in the excited $^2P_{3/2}$ state (as seen before in Fig. 2.1). Here a gray molasses cooling scheme [15] is applied, by which temperatures of $\approx 7\,\mu$K can be achieved in the BECK. From there the atoms are loaded into a magnetic trap, which traps the low-field seeking $|F, m_F\rangle = |1, -1\rangle$ hyperfine state. Its final temperature is $\approx 55\,\mu$K. The temperature rises because the cloud needs to be spatially compressed to allow for an efficient transfer into the dipole trap.

Condensation in the magnetic trap is not possible, because due to a negative background scattering length of $a_{bg} \approx -29a_0$, a resulting BEC would collapse in the process [16]. Therefore a Feshbach resonance of the $|1, -1\rangle$ state at $560\,$G [9] is employed. A magnetic field of

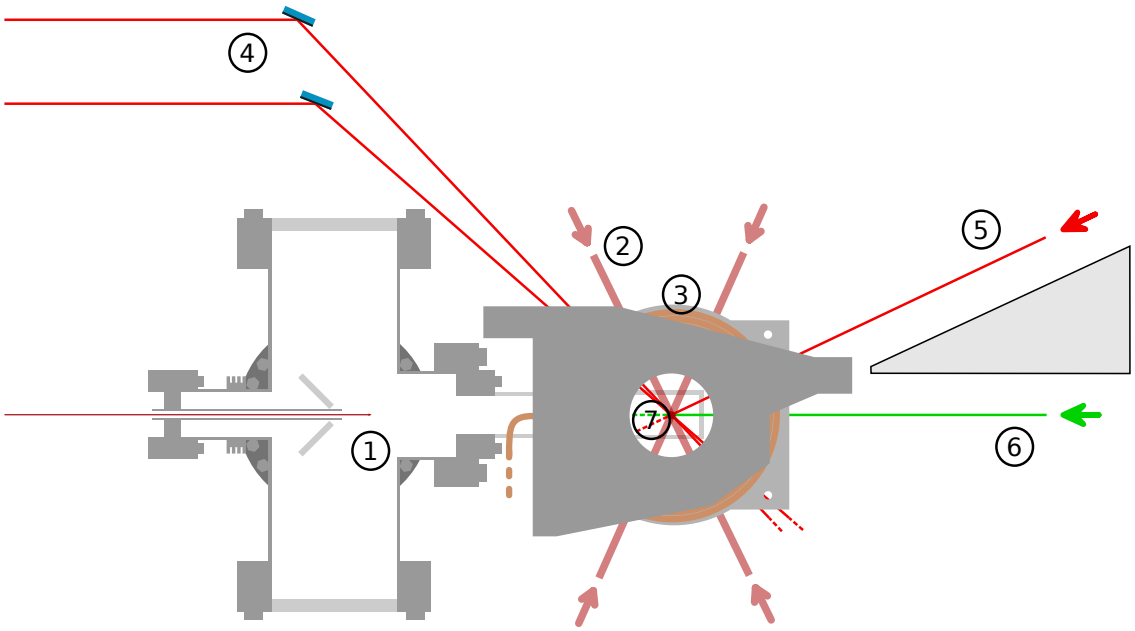

Figure 2.7 Schematic Overview of the experimental Setup (top-view). The beam of precooled atoms (1) from the 2D-MOT, loads the 3D-MOT (beams in plane (2)) inside the science cell (7). A gray molasses stage cools below the Doppler-limit, after which the atoms are loaded into a magnetic trap, produced by a pair of water-cooled coils (3). Two beams form the first and deepest dipole trap (4) in which condensation is achieved. A surfboard shaped compressor beam (5) raises the efficiency of loading the lattice (6). The objectives are omitted here, but would be on top and below of the science chamber (7). Image courtesy of Maurus Hans (BECK team).

$554.4\,\mathrm{G}$ shifts the scattering length to $a \approx 229a_0$. Condensation takes place in a red-detuned ($1064\,\mathrm{nm}$) dipole trap, by evaporatively cooling the atoms. It consists of two beams with $20\,\mathrm{W}$ each, resulting in a depth of $\approx 1\,\mathrm{mK}$, and an additional much weaker condensor beam approximately perpendicular to the others.

Roughly 3×10^5 atoms reach the condensate phase in the dipole trap, from where they can be transferred to the final trap geometry. To achieve this with minimal losses, an additional Kompressor beam is employed. This is a red detuned beam with a surfboard geometry, resembling the geometry of the final trap.

Final Trap

To get a 2D-geometry a vertical lattice of light sheets, that strongly confine the atoms in gravity direction, is produced. This is done similarly to an interferometer, by splitting a beam of coherent $532\,\mathrm{nm}$ light and letting the two beams interfere under a small angle in the trapping region (see Fig. 2.8). The angle is chosen such, that the resulting interference pattern produces a $5\,\mu\mathrm{m}$ lattice spacing. An additional Electro-Optic-Modulator in one of the beam paths allows for adjusting the relative phase between the two beams and can, therefore, be used to shift the pattern along gravity direction. For the planned $2\,\mathrm{W}$ of total beam power the setup will produce a potential of $\approx 1.7\,\hbar\mathrm{kHz}$ in vertical direction and $\approx 0.4\mathrm{i}\,\hbar\mathrm{Hz}$ and $8\mathrm{i}\,\hbar\mathrm{Hz}$ in lateral directions. The complex frequency denotes that its not a conservative harmonic potential in those directions, but falling of (proportional to the intensity) to the sides instead. For confinement in lateral directions the DMD will project arbitrary wall shapes with a planned potential height of $\approx 1\,\mathrm{k_B}\mu\mathrm{K}$. Like the lattice it shines in $532\,\mathrm{nm}$ light, but parallel to the normal vector of the lattice. The fact that both are blue detuned to the atomic transitions, as well as the large detuning, keeps scattering rates low (eq. 2.8), because the minimum of the potential is at the minimum of the lights intensity (eq. 2.7). This effect is most notable for deep potentials or steep walls ([8]) and is important to achieve low heating rates and long lifetimes for the BEC. Additionally the DMD could be used to compensate the declining potential on the flanks of the lattice with the use of grayscales (see. 3.2). It can also mitigate the perturbations the diffraction limited optics introduces in the form of higher orders of the projected walls (as will be shown in 3.2.2). Both compensations could be essential as can be seen for example in the Thomas-Fermi limit [17], where those perturbations would manifest themselves directly as ripples in the density.

Imaging System

At the end of the experimental cycle absorption imaging is performed at resonance with the atomic transition. To resolve the 2D-system, the $767\,\mathrm{nm}$ light is irradiated along its normal axis. Therefore imaging light has to overlap with the DMD light. This will be realized with a dichroic mirror, that is transmissive at $767\,\mathrm{nm}$ but reflective at $532\,\mathrm{nm}$ (see Fig. 2.8). From there both beams pass through an objective, which has its foci corrected for both $767\,\mathrm{nm}$ and $532\,\mathrm{nm}$, taking the thickness of the glass cell into account. An identical objective at the bottom is used to image the residual light onto the camera and will also be employed to reimage the DMD on another camera, to enable feedback of the applied potential. For that purpose the beam paths have to be split up again, which could be realized by another dichroic mirror. The

pair of objectives was made by Special Optics and have a numerical aperture of 0.5 with a backfocal length of $35\,\mathrm{mm}$.

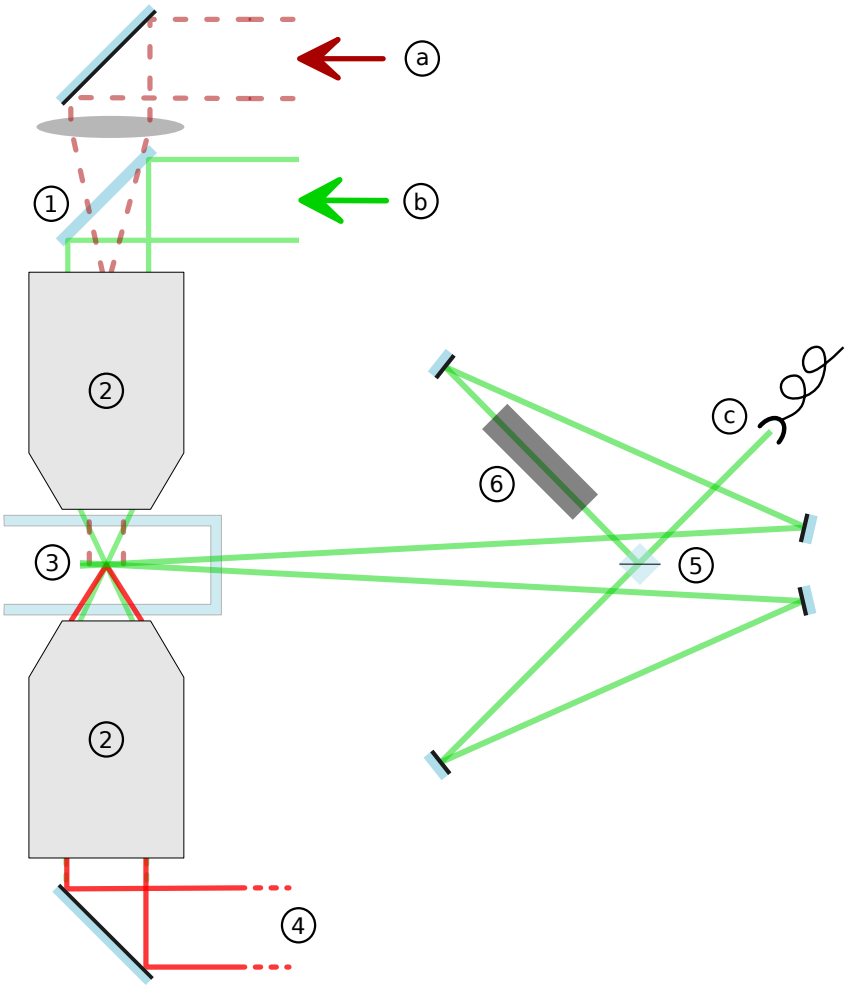

Figure 2.8 Schematics of the beam paths of the imaging (a), DMD (b) and lattice (c) (side-view) in the final trap. Imaging light and DMD light will be overlapped with a dichroic mirror (1) and pass through the objective (2) into the trapping region (3). An identical objective at the bottom enables reimaging towards the camera (4). Dashed lines in the imaging light denote the beam shape, whereas the solid lines, like for the DMD light, represent ray-traced like paths. For the lattice the beam (c) is split with a $50:50$ beam splitter (5) and interferes under a small angle in the trapping region (3). An additional Electro-Optic-Modulator (6) allows for adjustment of the relative phase between the beams and in turn to shift the resulting lattice.
Adapted from Maurus Hans and Celia Viermann (BECK-Team)

3 Feasibility Studies

To ensure that the setup can cope with the planned requirements, detailed feasibility studies were carried out in advance. Choosing a proper DMD chip and projection optics are not only essential to realize the primary application of box potentials, but also to leave options open for arbitrary potentials. Under the circumstances of diffraction-limited resolution and binary amplitude modulation, the capabilities of the setup to produce arbitrary potentials seem fairly limited. However, high resolution of the DMD can partly compensate this, even though its single mirrors are not resolved.

In this chapter, the chosen chip is briefly presented and properties essential for the application in the BECK experiment are discussed. After starting with the primary application of box potentials, it will be shown subsequently, how grayscales can be implemented in such a setup. Additional capabilities to produce high contrast edges like walls, while still keeping diffraction effects to a minimum, are also presented.

Two numerical calculations are employed, to get results for the planned setup. The first one calculates the resulting potential in the trapping region, which gives an insight into the required laser power and demagnification. The second concentrates on achievable potential shapes. It provides results for the implementation of grayscales, taking into account the predicted resolution of the optical system and the DMD. Furthermore, different wall shapes are investigated to reduce higher-order distortions in the potential. Although here results for the chosen resolution and chip size are presented, these numerical calculations played a role in the decision-making process, and were carried out for different DMD-chips.

DMD Chip and Controller Board

To have maximum possible freedom in the selection of the displayed patterns, the DLP9000X DMD was chosen. It has the highest available resolution (2560×1600 mirrors) with an individual mirror size of $7.6\,\mu\mathrm{m}$, which results in an active area of $19.4 \times 12.1\,\mathrm{mm}^2$.

The actual implementation with controlling hardware[1] was designed and built by ViALUX. It provides the features needed to ensure smooth operation with the other components. For example, it is shipped with an Application Programming Interface (API), which enables control with the programming language of choice. This includes MATLAB and Python (a Python API wrapper [18] was used throughout the work for this thesis). Connection to the controlling PC is enabled via USB 3.0. Additionally, stable mirror positions and precise timings during projection into the experiment are required to prevent any unwanted stray light from disturbing the potential. For this purpose, the controller board has external trigger capabilities at TTL voltages, instead of only having an adjustable framerate (up to $\approx 13\,\mathrm{kHz}$) with regular mirror clocking pulses (like described in 2.2).

[1] ViALUX V-9001

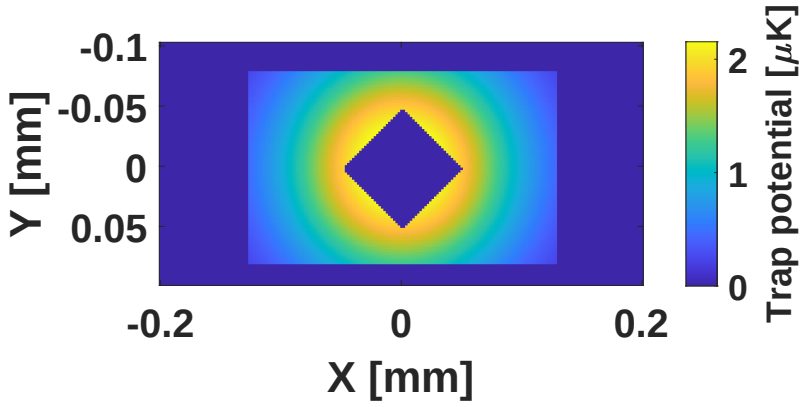

Figure 3.1 Numerically calculated potential in the atom plane of a square mask on the DMD with 1 W beam power. The incoming intensity has a Gaussian form with 140 µm width. Instead of the planned demagnification of 86, 76 was used (which results in a more conservative estimation). Nevertheless the potential is on the order of $2\,k_B\mu K$, which is sufficient, especially considering the beam power can be increased even further. Eq.2.7 was used to calculate the potential with a Matlab script.

3.1 Box Potential

To make use of the high resolution of the DMD, the demagnification of the reimaging had to be chosen such, that its resulting illuminated area in the atom plane matches the expected size of the BEC. Additionally, the height of the potential walls should be on the order of $1\,k_B\mu K$, to ensure sufficient trapping capability. Here a rough estimate for the expected area is presented. Subsequently, it is used to calculate the expected potential numerically. To get an upper bound on the size of the BEC, one can use the phase transition to the BEC, which is characterized by the associated critical temperature T_c. In the case of the experiment, achievable temperatures, atom numbers, and the dimensions in the direction of the lattice confinement can be estimated. An equation for T_c can, therefore, be adapted to calculate a critical area A_c, which is associated with the maximal extension of the atom cloud still allowing for the existence of a BEC:

$$A_c = \frac{N}{d\zeta(3/2)} \left(\frac{mTk_B}{2\pi\hbar^2} \right)^{-3/2} \tag{3.1}$$

With $N \approx 10^5$ atoms, $T \approx 100\,\mathrm{nK}$, the extension in lattice direction $d \approx 1\,\mu\mathrm{m}$, the mass of K^{39} $m = 38.96\,\mathrm{u}$ (taken from [9]) and the Riemann zeta function $\zeta(3/2) \approx 2.61$, this results in $26\,600\,\mu\mathrm{m}^2$ or a side-length of $163\,\mu\mathrm{m}$ for a box shape. This is only a rough estimate as it assumes no interactions and constant temperature during the expansion in the lattice. Additionally, this is for negligible losses and at the point of the phase transition.

In practice, the boxes will be smaller as a demagnification of 86 was chosen (see 4.2). The short axis of the active chip area, therefore, has a size of $\approx 140\,\mu\mathrm{m}$ in the atom plane. Higher demagnification leaves more room for grayscales (which will be shown subsequently) and reduces the necessary total laser power for a given trap depth.

To quantify the potential a numerical calculation was adapted for the DMD setup, which was originally developed by the BECK team to calculate the potential of the dipole trap. It employs eq. 2.7 with values for the natural linewidth $\Gamma/2\pi = 6\,\mathrm{MHz}$ and wavelengths $\lambda_{D1} = 770.1\,\mathrm{nm}, \lambda_{D1} = 766.7\,\mathrm{nm}$ taken from [9]. Although for the DMD light being at $532\,\mathrm{nm}$, the resulting detunings $\Delta_{1/2}$ are so large that even the two-level approximation would be justified, only the hyperfine splitting of the ground state (see Fig. 2.1) has been neglected additionally. Fig.3.1 shows the results for a square potential of $70 \times 70\,\mu\mathrm{m}^2$ in the atom plane and $1\,\mathrm{W}$ beam power (including the discarded power in the dark regions). Even for larger box sizes, the required height of the wall potential could still be achieved. Along the short axis, the gaussian shaped potential does not drop under $1\,\mathrm{k_B}\mu\mathrm{K}$.

3.2 Potential Shaping

3.2.1 Grayscales

To produce adjustable intensities (grayscales) from a binary SLM, one can either use the effect of inertia of the sensor (time-averaging), or the limited spatial resolution of the sensor (spatial-averaging) if the SLM performs better in one of those categories. Commercial applications of DMD's typically use the switching rate, often combined with modulation of the illumination. For example, to get an additional value of 0.5 from the binary options, it displays the image twice, once with the mirrors in ON- and once in OFF- position for all the gray pixels. In the time-average, this results in the desired grayscale at the expense of half the frame rate. Although some DMDs can reach more than $20\,\mathrm{kHz}$ switching rate, this can very well still be a limiting factor. For example, producing 8-bit grayscales by mirror-flipping alone cuts down the frame rate by a factor 255, which results in less than $80\,\mathrm{Hz}$. While this may be enough for the human eye not to notice any flickering, this is not the case for the BEC. Experiments with a BEC of ^{87}Rb showed that heating of the atoms emerged for frame rates lower than $\approx 3\,\mathrm{kHz}$ [19]. Because of the lower mass number of ^{39}K, heating is expected to set in at even higher frequencies, rendering the time-averaging technique not feasible for the experiment.

Instead, grayscales are implemented with a spatial-averaging technique, using the limited resolution of the output optics. For two neighboring mirrors being unresolvable, it virtually does not matter which one is turned on. In that case, one can group the mirrors in 2 by 2 patches. This results in four grayscale values, depending on how many of the mirrors are turned on, at the cost of a factor two in the resolution of each axis. While this is not the way to implement grayscales for most use cases like video projection, where high resolutions are desired, large demagnification to the atom plane is needed in the experiment, which results in the individual mirrors being unresolvable.

In principle, one could now build patches below the resolution limit of the last objective. From there, one would downscale the pattern to the resulting lowered resolution and round every pixel to the nearest available grayscale value. In the planned setup the minimal resolvable distance corresponds to $\approx 7\,\mathrm{mirrors}$, demagnified to the atom plane. This results in almost 50 available grayscale values.

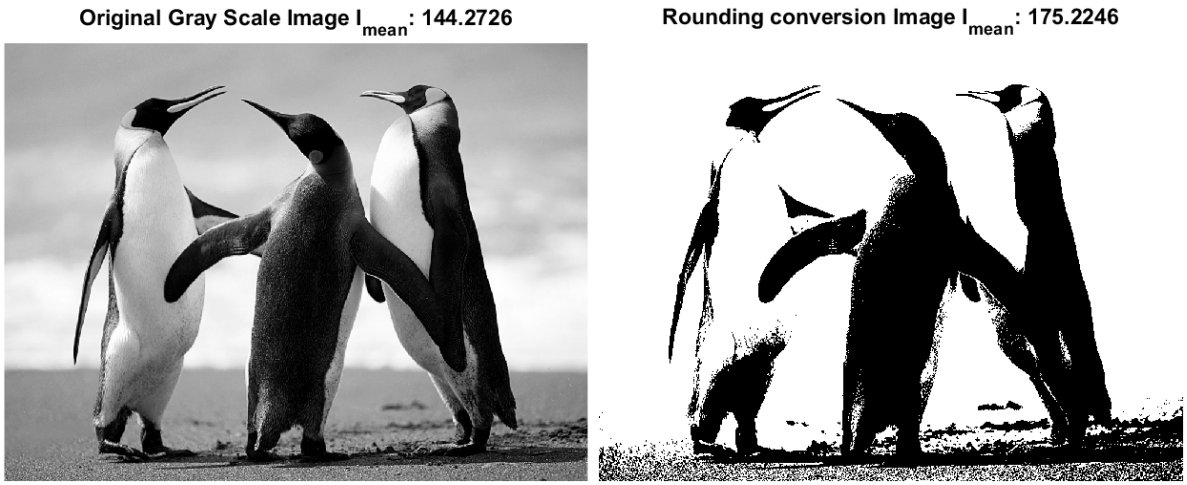

(a) (b)

Figure 3.2 Original gray scale image (a) and rounded to binary (b). The mean intensity went up from 144 (in 8-bit ranging from 0 to 255) to 175. Also large areas turned out either completely white, like the background and the penguins torsos, or completely black, like their backs. Picture taken from Microsoft [20].

Floyd-Steinberg Error Diffusion

Fig. 3.2 illustrates the fundamental problem that arises while implementing grayscales by rounding the original distribution to the nearest available grayscale value. Without consideration of the rounding errors, large areas that had intensity gradients before are rounded to the same value. In the worst case, the overall intensity also gets significantly altered. Although the given example rounds to binary, which is an extreme case, these effects persist for any limited number of grayscales.

To account for the error made by rounding, it first has to be calculated by taking the difference of the rounded pixel and the original one. Subsequently, this error can be redistributed to surrounding pixels. One algorithm that does this is the Floyd-Steinberg error diffusion algorithm (FS-algorithm) [21]. For every pixel $*$ that is rounded, the error is redistributed via the kernel:

$$\begin{bmatrix} & * & \frac{7}{16} \\ \frac{3}{16} & \frac{5}{16} & \frac{1}{16} \end{bmatrix} \tag{3.2}$$

The weights are chosen such, that for a gray value of 0.5, the resulting binary picture is a checkerboard pattern. Note that this algorithm leaves already rounded pixels untouched, meaning one has to sweep through the image only once. This makes it computationally efficient. The implementation programmed for this work sweeps through the pictures in a serpentine fashion, alternating between left-to-right and right-to-left sweeps for every row of the picture (with mirrored kernel for right-to-left). This should help reduce the effect of errors being redistributed over vast distances when areas of black or white do not allow for compensation. Fig. 3.3 shows the results for the picture rounded earlier. Not only are the overall intensity errors much smaller, but also more of the original structure in the image is preserved. Transforming the image to binary with this algorithm also replaces the need for

Figure 3.3 Grayscale picture from 3.2 rounded to binary with the error diffusion algorithm of Floyd and Steinberg. The fact that the error is diffused locally does not only conserve overall intensity (144), but also preserves some of the local structure as can be seen by comparing to the rounded version.

building patches in the first place. However, it does not invalidate the underlying limits arising from the resolution limit of the optics. For gray values lower than those limits, the algorithm will still work, and the resulting pattern will have some pixels turned on. However, because their distance is at resolvable scales of the optics, this will not result in the uniform gray value that was intended, but bright spots being visible, instead.

Numerical Results for the Experiment

The number of available grayscales is directly tied to the number of pixels under the resolution limit. This is the main reason the highest available resolution of $2560 \times 1600\,\mathrm{px}$ with a mirror size of $7.6\,\mu\mathrm{m}$ was chosen. With an numerical aperture of 0.5 of the objective, the resolution limit is $d_{min} = 1.22\lambda$ (eq. 2.26), while the dipole potential is generated with $532\,\mathrm{nm}$ light. For a demagnification of 86, this results in ≈ 6 mirrors within one wavelength in the atom plane.

Taking these parameters into account, the intensity in the atom plane can be calculated for any intensity distribution in the plane of the chip. First, the field distribution in the plane of the chip $f(x, y)$ is assumed to be the square root of the intensity distribution (see eq. 2.14) and gets upscaled by a factor 10 for better visibility in the atom plane. The intensity after the output optics can then be calculated by folding the $f(x, y)$ with the field-PSF (see 2.4.1), and squaring the result. For this, the field-PSF (eq. 2.25) is rescaled such that $d_{min} = 1.22 \times 6\,\mathrm{mirrors}$ and evaluated on a $25 \times 25\,\mathrm{mirror}$ grid.

The calculation can now be tested on the grayscale picture, binarized with the FS-algorithm. A small area of $200 \times 200\,\mathrm{px}$ around the head of the right-most penguin is transformed, both for the original and the FS-binarized picture. The input pictures and the resulting output can be seen in Fig. 3.4.

While the overall shapes look similar, the spatial intensities do not, which also reflects itself in the mean intensities. These differences arise due to the non-linearities in the calculation, more precisely taking the square or the inverse. While the FS-algorithm redistributed the intensities, the field-PSF alters the field distribution. To test this further, the square root of the original picture was binarized, resembling the field distribution. In this case the resulting output has roughly the intended intensity (see Fig.3.5).

For single mirrors being unresolved, their field-PSFs interfere in the atom plane. Therefore many mirrors contribute to the field at a given point in the atom plane. Summing up those contributions (superposition principle) and squaring to get the intensity, substantially differs from summing up the intensity contributions of the single mirrors. For a point in the atom plane, to which mirrors of a region contribute by the same amount (neglecting the actual shape of their field-PSFs), the intensity in the atom plane is proportional to the fraction of mirrors in the ON-state in this region squared. However, for single mirrors being resolvable, this is not the case, as for large distances the overlap between the field-PSFs decreases substantially.

Taking a look at regions in Fig. 3.4 in which the intensity varies only slowly, for example, in the background, a disadvantage of the chosen FS-algorithm becomes visible. For constant gray values, it produces regular patterns, which can produce structures in the atom plane although those are still much smaller than the clearly visible higher orders of the PSF in regions of high contrast or at the edges of the pictures.

3.2.2 Diffraction Effects on Walls and Edges

Besides grayscales, the quality of high contrast edges can also benefit from high resolution of the DMD, as it allows for a trade-off between wall steepness and small higher diffraction orders, resulting from the diffraction-limited optical system. This may also be needed for the potential walls, where one wants to prevent those higher orders from ending up inside the dark region.

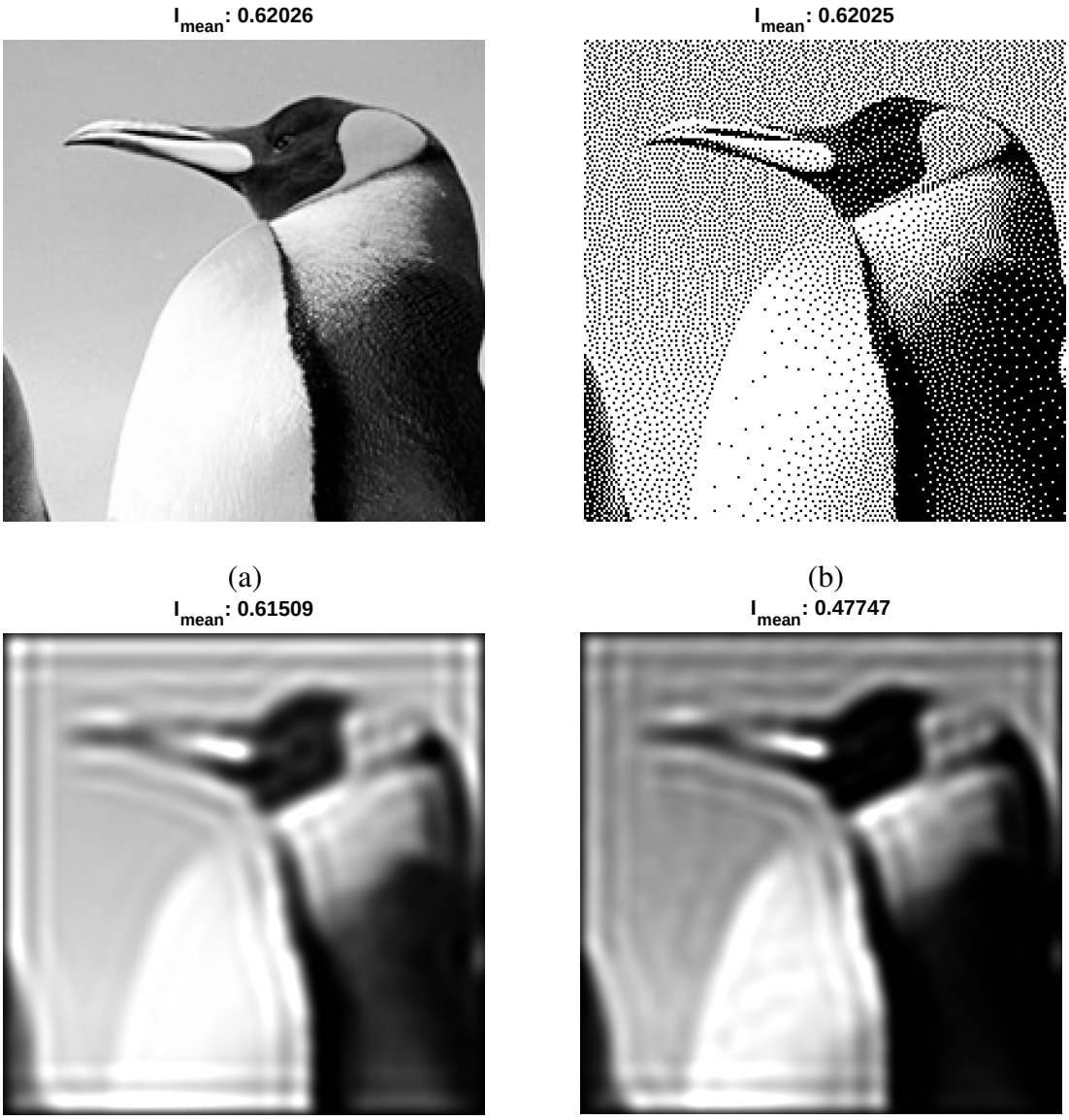

Figure 3.4 Numerical results for the intensity distribution in the atom plane (c and d), for a grayscale intensity distribution (a) in the plane of the chip and the binarized version (b). A comparison between the c and d reveals, that the FS-binarized version (d) produces additional structures in areas where the output of the original picture (c) is smooth. Higher orders of the PSF are visible in both, for regions of high contrast. Although the intensities in the plane of the chip are the same, they strongly differ for the atom plane. Note that this is not a representation of a picture displayed by the whole DMD chip, but of a small area of $200 \times 200\,\mathrm{mirrors}$ only.

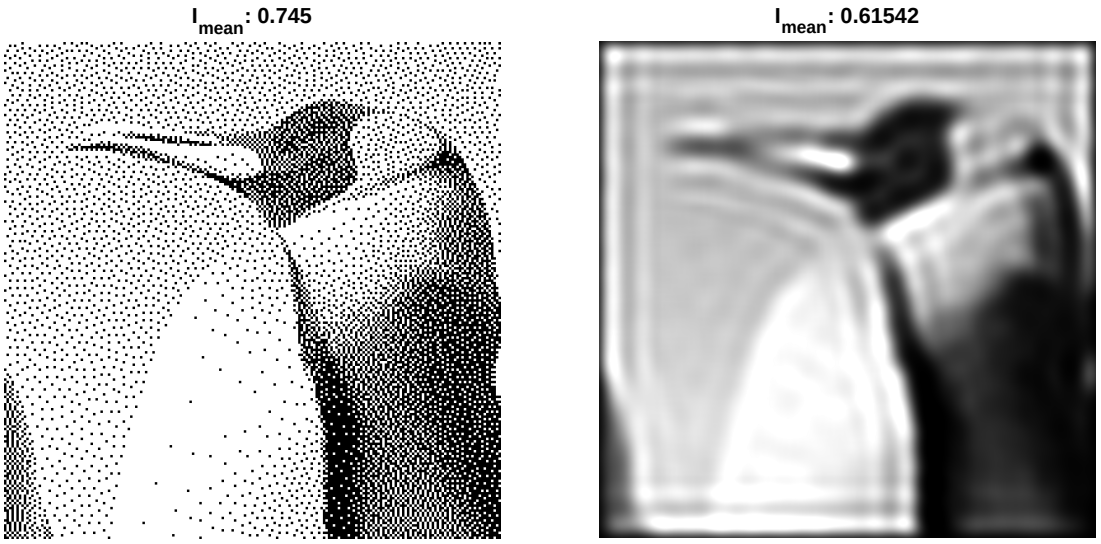

(a) (b)

Figure 3.5 Numerical results like in Fig.3.4. For FS-binarizing the square root of the original gray scale picture (a), which is proportional to the field, the intended intensity is aquired in the output plane (b). This is the case, because a flattened field distribution of (a) resembles the field distribution of the original gray scale picture.

High resolutions present the opportunity to break up the step function shape of the wall. Instead of having all mirrors in the ON-state on one side and all mirrors in the OFF-state on the other, one can define a border region where only some of the mirrors are turned on. These patterns can be chosen such that the higher orders of the field-PSF interfere destructively, which reduces the field and resulting intensity inside the black region.

As a proof of concept, in a 1D implementation of the numerical calculation described above, all possible combinations for 7 mirrors next to the wall have been tested (with the 8^{th} directly at the wall being always on). Here the wall consists of 100 mirrors, and again 6 mirrors are within one wavelength. Fig. 3.6 shows a comparison between the best result and the unaltered wall. For the optimized version, the pattern was $[10110001]$ with the last one representing the mirror at the wall. Although this pattern had the smallest undershoot (first order in field), many more combinations lead to similar results. While this first higher order is much smaller than for the unaltered wall, the detrimental effect on the wall steepness is also visible. This is the trade-off one makes by removing the highest available frequencies from the wall. However, this allows for better configurations overall, as the intensity is variable.

Results for the intensity in 2D, calculated with the original implementation, can be seen in Fig. 3.7. Here two walls, the left one with the optimized pattern and the right one unaltered, are shown next to each other. Each wall consists of 100×100 mirrors. Their distance is at $50\,\mathrm{mirrors}$ chosen such, that with the cut-off after $25\,\mathrm{mirrors}$ for the evaluation of the field-PSF their fields can not interfere. A 1D cut through the plane is also shown (Fig. 3.8). Especially in the zoomed-in version one can see the difference between the unaltered wall (orange) and the optimized one (blue), whose higher orders are still barely visible.

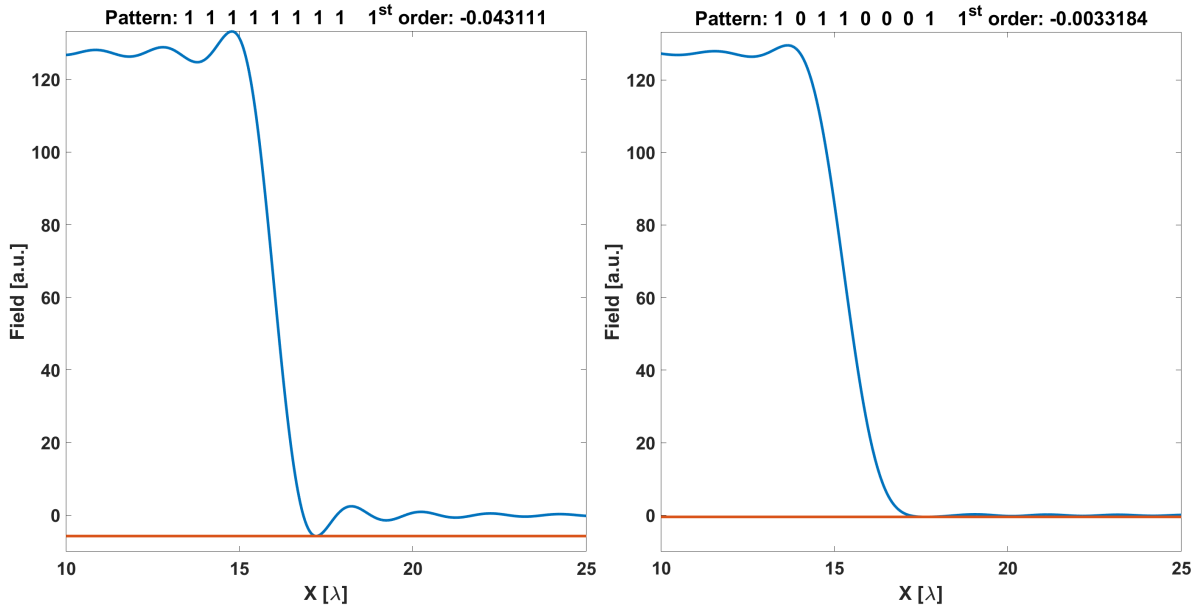

(a) (b)

Figure 3.6 Numerical calculation for different wall shapes in search for patterns that result in destructive interference of higher orders. The wall consists of 100 mirrors with $1/6$ of a wavelength each. All combinations of the 7 mirrors next to the wall have been tested. (a) shows the unaltered wall shape with all mirrors on and (b) shows the best combination found, where the higher orders interfere destructively. The quality was determined by the undershoot of the first order, relative to the maximum. While the normal wall has 4.3% of the maximum field in the first order, this value is reduced by more than a factor ten in the optimally shaped wall (0.33%).

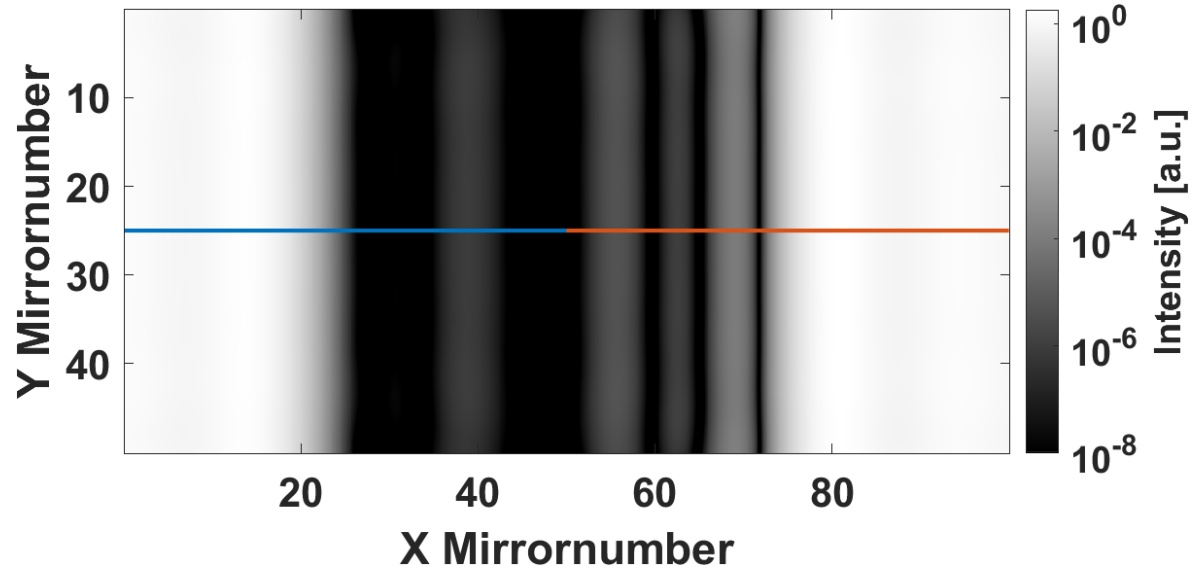

Figure 3.7 2D results for the best pattern found in 1D (left) and unaltered wall to compare (right). Note that here the logarithm of the intensity is shown for better visibility of the higher orders. A cut through the middle of those walls for comparison is denoted with the blue and orange lines and can be found in 3.8

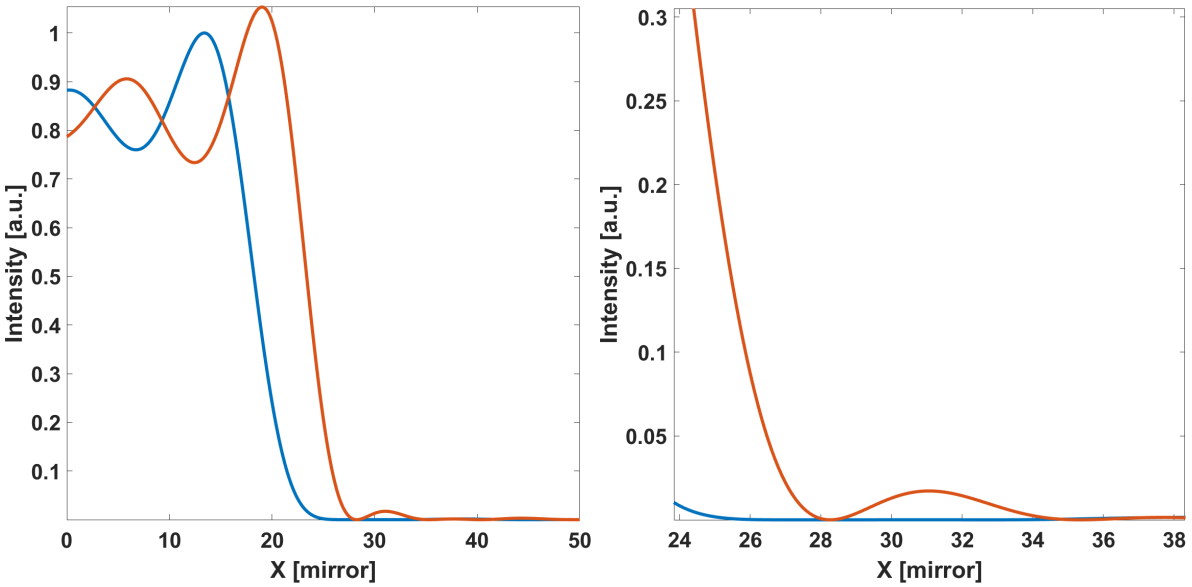

(a) (b)

Figure 3.8 Cut through the wall in fig. 3.7. The blue line shows the optimized pattern and the orange one the unaltered wall. While for the unaltered wall the difference in steepness is visible (a), the zoom in in (b) illustrates the striking difference in intensity for the higher orders. This is the trade-off one has to make in general when optimizing for less light in the dark areas by destructive interference. Those results are not directly transferable to the patterns used in the experiment, but show the availability of such optimization.

Even though those results look very promising, they are not directly transferable to the experiment for multiple reasons. First and foremost, the PSF is only to first-order an Airy disc (an extreme example can later be seen in fig. 5.3). Not all apertures are perfectly circular and aligned on a common axis. In particular, the mirrors themselves are at different distances from the beam axis. Additionally, their light is not perfectly in phase and of slightly varying amplitudes, even for mirrors close to each other. In case of walls that are not aligned with the rows or columns of the mirrors on the chip, also the effective distance between the mirrors along the wall is different. The combination of all these factors introduces an ambiguity in the process of calculating the intensity in the atom plane, which significantly limits the possibilities to calculate the optimized patterns beforehand. To overcome this, in 5.2, an automated procedure is presented, which could find those patterns in the experiment by switching mirrors and analyzing the resulting picture taken by a camera.

4 Test Setup

With the requirements set and, most importantly, the DMD chosen, this chapter describes the test setup. The description in the following sections is closely tied to the optical path. Therefore the illumination optics are presented first, and the output optics subsequently. Although some parts in the output optics, for example, the objectives, are used exclusively for testing and will not be part of the final setup, most of it will be transferred to the experiment. In the end, measurements and observations acquired during and after build-up are shown.

4.1 Illumination Optics

Light Preparation

Most of the lights in the BECK is prepared on a separate optical table and transferred to the experimental table via fibers, including the $532\,\mathrm{nm}$ light. Stabilized power up to $2\,\mathrm{W}$ is required after the fiber. This is achieved using an Acousto-Optic Modulator (AOM), used for the adjustment and stabilization, and a high-power fiber[1], capable of transmitting several Watts. In Fig. 4.1 schematics of the setup are presented.

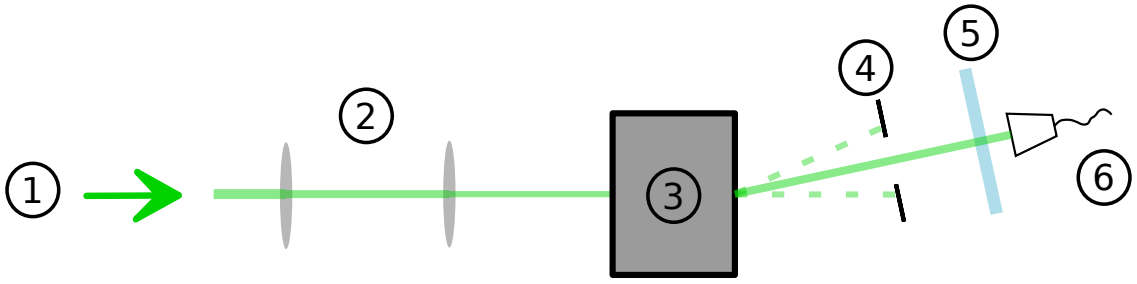

Figure 4.1 Schematics of the light preparation. The laser light, coming from (1) is narrowed with a telescope (2) and diffracted by an AOM (3). The first order is coupled into a the high power fiber (6), while all others are blocked by an iris (4). An additional half-wave plate (5) matches the polarization to the polarization maintaining axes of the fiber.

The $532\,\mathrm{nm}$ laser[2] used, has a maximal output of $7\,\mathrm{W}$ and is used for the vertical lattice as well. After splitting the power between the two the beam is narrowed with a telescope (2) to better match the aperture of the AOM (3). It diffracts the beam into several orders by producing a grating with sound waves in a crystal. Because the amount of light diffracted depends on the intensity of the sound waves, this enables power adjustment and stabilization. As seen for the blazed grating, output power in a given order depends on the angle of illumination.

[1] Photonic crystal fiber made by NKT Photonics
[2] Verdi-V10

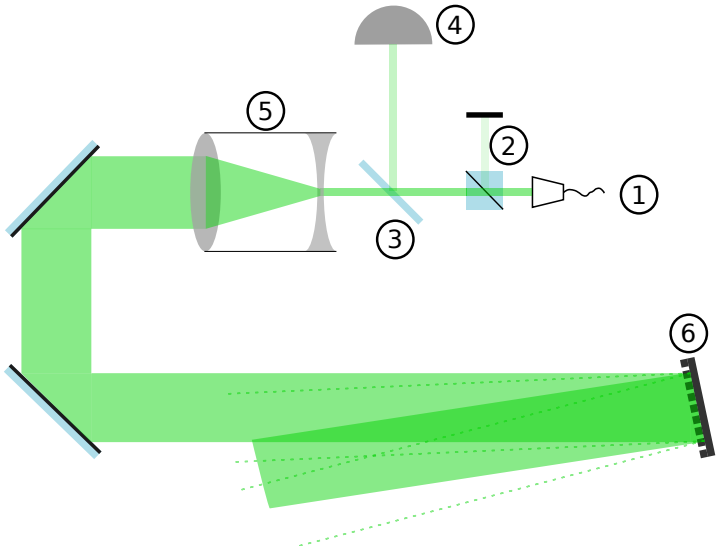

Figure 4.2 Schematics of the illumination optics. Right after the fiber coupler (1) a polarizing beam splitter (2) cleans the polarization. Afterwards a pickup plate (3) reflects a fixed fraction of the power on a photodiode (4) to measure the total power. All these components are mounted in a cage system. After this the beam is widened with a Galilean telescope (4) to fit the size of the short axis of the DMD chip (5).

It is adjusted such that the first order is maximized. By choosing the opposite order in the setup of the lattice (see. 2.5 and Fig. 2.8), interference between the beams is prevented. This can be done, because the AOM shifts the frequency of the laser by that of the sound waves ($\approx 80\,\mathrm{MHz}$). After blocking all but the first order with an iris, the beam is coupled into a high power fiber. This is done in a polarization maintaining way. Therefore the polarization of the laser is matched with the corresponding axis of the fiber with an additional half-wave plate (5).

Illumination of the DMD

On the experimental table additional optics is needed for illumination of the chip. The beam size has to be adjusted such that it illuminates the whole short axis of the chip. Additionally a power measurement is established, which allows to make use of the AOM's power adjustment capabilities. A schematic view of the setup can be found in Fig. 4.2.

After the light is coupled out of the fiber (1), it is polarization cleaned with a polarizing beam splitter (2). This ensures that only linear polarization is left and the resulting dipole force in the trap shifts all magnetic sublevels equally (see. 2.1). A subsequent pickup plate (3) couples out a fixed fraction of the beam power ($\approx 5\%$), that is then measured with a photodiode (4). Its output voltage, which is proportional to the beam power, is used as the input for a proportional-integral (PI) controller, whose output is connected to the AOM controller. This way a control loop is established, which ensures a stable power. The target value for the PI controller can then be set by the controlling PC to adjust the power. Parts (1) to (4) are mounted in a cage system, which ensures alignment and compact design and eases the transfer to the final setup. To fit the size of the DMD, the beam is widened with a Galilean telescope (5)

consisting of a $-25\,\mathrm{mm}$ and a $200\,\mathrm{mm}$ lens resulting in a total magnification of 8. This leads to a beam diameter of $\approx 12\,\mathrm{mm}$, which ensures illumination of the whole short axis of the DMD-chip (6) ($\approx 19.4\,\mathrm{mm} \times 12.1\,\mathrm{mm}$). It is then illuminated under $\approx 24°$ with respect to its normal axis.

Chip Mounting

As mentioned previously the chip is mounted vertical to the table but turned by an angle of $45°$ to have all the optical paths parallel to the table. Another important factor was to ensure that the output optics is aligned with the normal vector of the plane of the chip. With an additional translation along this axis the plane of the chip can be aligned with the focal plane of the output optics. To implement this alignment of the chip, it is mounted on a 5-axis translation stage[3]. This was realized utilizing a self-designed mount (Fig. 4.3), which was made out of aluminum by the institutes workshop. Aluminum has a high thermal conductivity, which is important because the chip can dissipate up to $11\,\mathrm{W}$ electrical power, not even taking additional heating by the laser into account.

Ideally the blaze condition should be met to have the highest power possible in the main diffraction order (like discussed in 2.3). However, for the chosen mounting angle (and wavelength) this can not be realized. Output angle $\beta = 0°$ and mirror tilt $\theta = 12°$ already define the illumination angle $\alpha = 24°$ according to the condition for constructive interference of the single mirror (eq. 2.9). Because the whole chip is much larger than its single mirrors (leading to the smaller structure in Fourier space) its interference condition (eq. 2.10) is the more relevant of the two. Satisfying it, the closest one can get to $\alpha = 24°$ for the output $\beta = 0°$ is $23.3°$ (Note that, because of the mount at $45°$: $d = \sqrt{2} \times 7.6\,\mu\mathrm{m}$). If however, in future applications, power should be the limiting factor, one could for example illuminate under $\alpha = 29.8°$. Then the blaze condition is met at $\beta = -5.8°$, while the optical paths can be kept parallel to the table. A picture of the diffraction orders that arise after the DMD can be found in Fig. 4.4.

4.2 Output Optics

The output optics need to demagnify the displayed patterns to the atomic plane and have to deal with the grating nature of the DMD-chip. Because the demagnification is large, it is split up into two 4f-systems. This setup was chosen, because the beam is collimated in between the 4f-systems. Additionally an iris in the first 4f-system is employed to block other orders as well as stray light scattered from the vicinity of the chip. Fig. 4.5 shows the schematics of the setup.

The desired demagnification of the system is ≈ 90 and the effective focal length of the objective is fixed to $35\,\mathrm{mm}$. This would result in a path length of over $6\,\mathrm{m}$ for a single 4f-system. Although a distance of at least $50\,\mathrm{cm}$ is needed between the lens and the objective for the final setup, this is not feasible. Therefore, the first 4f-setup (2 & 4) has a demagnification of 4, which reduces the optical path needed for the second 4f-setup (6 & 7). It consists of a $200\,\mathrm{mm}$ (2) and a $50\,\mathrm{mm}$ (4) achromatic doublet lens, which is a trade-off between reasonably slow lenses and short optical path. The remaining demagnification of 22.5 is then realized

[3] Newport 9081-M

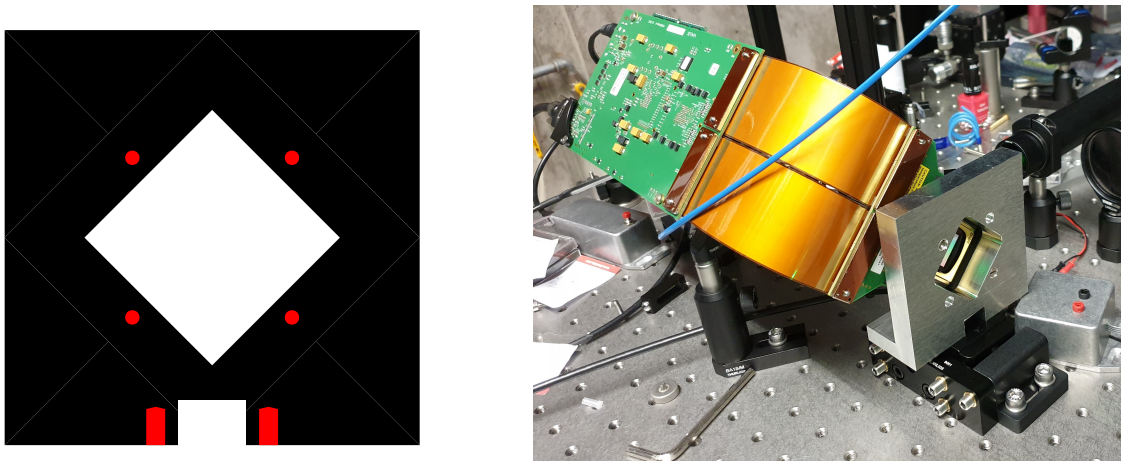

(a) (b)

Figure 4.3 Front view of the schematics (a) and picture (b) of the DMD mount on the 6-axis translation stage. The mount is designed such that the chip is held on its heatsink and screwed at four points to the translation stage. This allows for alignment of the plane of the chip to the focal plane of the output optics. The mount was made out of aluminium by the institutes workshop. Due to the stiffness of the connecting ribbon cables, the controller board (green) had to be mounted at $45°$ too.

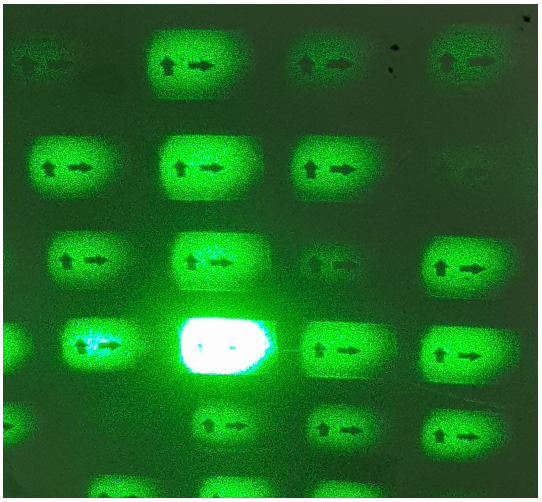

Figure 4.4 Picture of the diffraction orders on a screen after the DMD without any output optics. One can see side-orders stemming from the grating nature of the chip. The main order is oversaturated for better visibility of the side-orders.

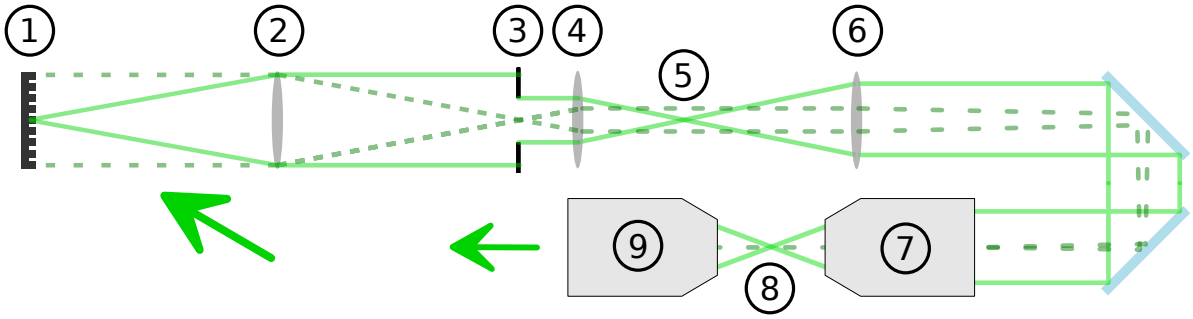

Figure 4.5 Schematic of the output optics in the test setup. Dotted lines illustrate the beam shape, whereas the solid lines represent a ray-trayced like path. Right after the DMD chip (1), the first 4f-setup (2 & 4) demagnifies by four in the intermediate image plane (5). An additional aperture (3) blocks stray light. A second 4f-setup, consisting of a lens (6) and the objective (7) provides further demagnification for a total of 86 in the test plane (8). An additional microscope objective (9) is used to reimage on the camera. An advantage of using two 4f-setups is that the beam is collimated at the two image planes (5 & 8).

with a $750\,\mathrm{mm}$ lens (6) and the objective (7) in the second 4f-setup. Since the final objective could not be used for testing, a similar one was used. It has a smaller numerical aperture of 0.3 as compared to the 0.5 of the final objective. Its effective focal length of $35\,\mathrm{mm}$ ensures comparability to the final setup. Together with the $750\,\mathrm{mm}$ lens, it demagnifies the image further by 21.4 resulting in a total demagnification of 86.7 for the projection system as a whole.

This gives a lower bound for the opening of the iris (3), not making it the limiting factor for the numerical aperture of the projection optics. While going in beam direction demagnifies the beam size in real space, it magnifies the beam size in reciprocal space. Therefore one needs to consider the last lens of the first 4f-setup with $50\,\mathrm{mm}$ and the $750\,\mathrm{mm}$ as a telescope in Fourier space, resulting in a magnification of 15. For an exit pupil of the objective of $35\,\mathrm{mm}$, the iris should therefore be operated at openings larger than $2.3\,\mathrm{mm}$.

To reimage the resulting image in the test plane (8) with a camera[4], an additional microscope objective is used to magnify by 10. It has the a aperture of 0.2 only and is therefore the limiting factor in setup. While this limits the resolution of the camera images of the test plane, characterization and optimization procedures work the same. In the final setup both objectives are identical. The next section presents images taken from the intermediate image and the reimaged test plane.

[4]Mako G G-223B NIR

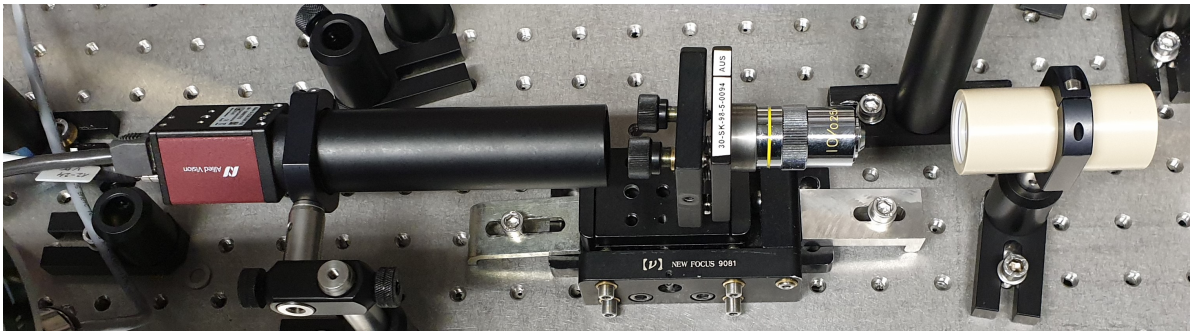

Figure 4.6 Picture of the objectives in the test setup. From right to left, the beam passes through the homebuilt objective (beige), which is the replacement for the final objective and has a smaller numerical aperture of 0.3. To reimage the resulting intensity distribution in the test plane and additional microscope objective with a magnification of 10 and numerical aperture of 0.2 is used. Afterwards, an image is taken with the camera (red). The microscope objective is mounted on a translation stage to make alignment easier. The lens tube in front of the camera reduces stray light on the camera chip and does not contain any additional optics.

4.3 Results and Observations

To monitor the building process and check the alignment tests of the setup have been performed throughout the building process and in its final configuration shown above and are presented in the following. First pictures from the intermediate image plane, as well as the reimaged test plane are shown. Those pictures are used to infer the demagnification of the setup. A test of the resolution is realized and multiple observations are shown, for example the effects of an uneven phase profile of the beam after the DMD.

Demagnification

Fig. 4.7 shows images of both image planes. To infer the demagnifications the sizes in pixels of the originally shown pattern and the camera image got compared. The different pixel diameters of $7.6\,\mu\mathrm{m}$ for the DMD mirrors and $5.5\,\mu\mathrm{m}$ for the camera pixels need to be taken into account. For the reimaged pattern the magnification of the microscope objective of 10 is respected additionally. It was taken to be exact. The resulting demagnifications are 4.04 ± 0.05 for the intermediate image and 89.9 ± 2.3 in the test plane. Both these values are consistent with the planned ones of 4 and 86.7. The uncertainties stem from the ambiguous assignment of the edge pixels.

Resolution

The resolution of an optical system can be measured in multiple ways. Although the Rayleigh criterion (eq. 2.26) defines it as the minimum distance between two spots to be resolvable, many tests employ the fact that this is set to the distance between the maximum and the first minimum in the PSF. Usually it is preferable to measure the PSF of a single spot, than to produce two spots of adjustable distance. This is, at least in discrete steps, easy to implement with the DMD. However, because coherent light is used and therefore the spots field-PSFs

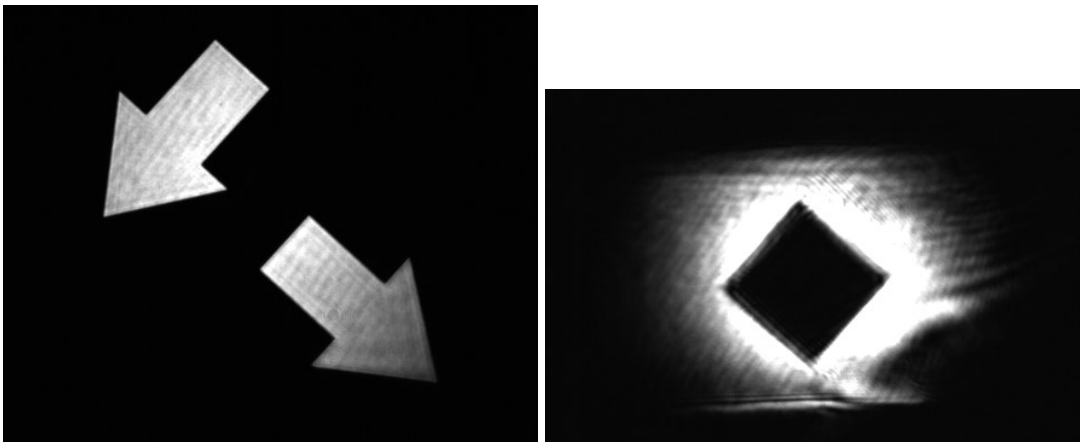

(a) (b)

Figure 4.7 Pictures of two arrows in the intermediate image plane (a) and of a box in the reimaged test plane (b) used for determination of the demagnification. The feature in the bottom right of (b) stems from residual clipping in the early alignment stage this picture was taken in. Nevertheless unevenness in the intensity profiles, which go beyond the Gaussian illumination profile, can be seen in both pictures.

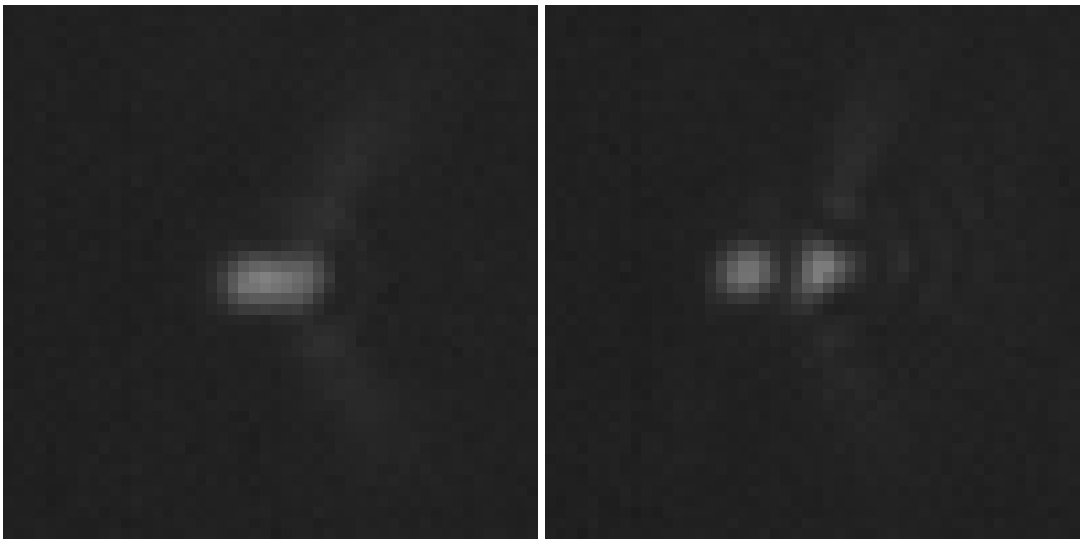

(a) (b)

Figure 4.8 Reimaged pictures of two spots for different distances between the spots, to measure the resolution limit. Each spot consists of a 16 by 16 mirrors patch on the DMD. In (a) the original patches are seperated by 16 mirrors ($1.35(3)\,\mu\mathrm{m}$ in the test plane), those in (b) by two times that. Somewhere in between is the resolution limit. Further investigation using this approach is difficult, because the field-PSFs interfere as visible in (b), where the right spots main order is visibly distorted.

interfere, it is hard to make a reliable statement for the smallest resolvable distance (see. Fig. 4.8).

Instead, Airy discs were fitted to the PSFs of over a hundred spots distributed over the DMD. An Airy disc with scaling factor a was used as fitting function:

$$I(r) = I_0 \left(\frac{J_1(\pi r/a)}{\pi r/a} \right)^2$$

Its first zero is at $r_0 = 1.22a$ (following eq.2.25). The spots were post-selected, excluding points with a fitted intensity over the cameras saturation. a was found to be $4.67(13)\,\mathrm{px}$, where the error is the standard deviation of the fitted a values. Multiplying the corresponding r_0 by the pixel size of the camera ($5.5\,\mu\mathrm{m}$) and dividing by the magnification of the microscope objective (10) yields the resolution in the test plane: $d'_{min} = 3.13(9)\,\mu\mathrm{m}$.

However, this does not include the size of the spots, which where made out of 16 by 16 mirror patches. Technically, one needs to deconvolute the measured spots with the demagnified patch to get the PSF (see eq. 2.24). As an estimate the sidelength of $1.35(3)\,\mu\mathrm{m}$ in the test plane (with the error of the demagnification) is subtracted instead:

$$d_{min} = 1.78(9)\,\mu\mathrm{m}$$

Using eq. 2.26 the corresponding numerical aperture can be calculated. The resulting $0.182(11)$ is consistent with the specifications of the microscope objective.

Additional Observations

Finally, some additional observations like an uneven phase profile of the beam after the DMD and ghost-like images in the intermediate image plane are presented. Those ghost-images were first observed while examining the influence of the iris on the intermediate image. For this the exposure of the camera was set such, that the images were oversaturated, which results in a better visibility of stray light and diffraction orders. There, those ghost images appeared, which resemble the original images closely, but appear with slightly different size and seemingly random positions. Fig. 4.9 shows the influence of the iris as well as a highly oversaturated picture of the ghost-images. Although they are clearly visible there, they are dim in comparison to the images themselves. Analysis of pictures taken with different exposure times showed, that the intensity of the brightest of these ghost-images is on the order of 1% of that of the images. Also an enhanced stability of the ghost-images against defocussing as well as strong dependence on the angle of the last lens was observed. This led to the believe that the ghost-images are reflections at this lens. Since they do not share the optical path with the original images, they should not propagate to the test plane. This was confirmed as no such features have been observed there.

Instead, during buildup of the second 4f-system, a beamshape far off the expected gaussian profile, has been observed between the two 4f-systems. Fig. 4.10 shows the beam profile after the DMD with all mirrors in OFF-position after a few meters of free space propagation. This rules out alignment errors of the 4f-system and results in the same pattern, but bigger. Apparently the DMD induces phase distortions, which manifest themselves in a bad beamshape. Those aberrations arise from the chip not being perfectly planar and are well known from

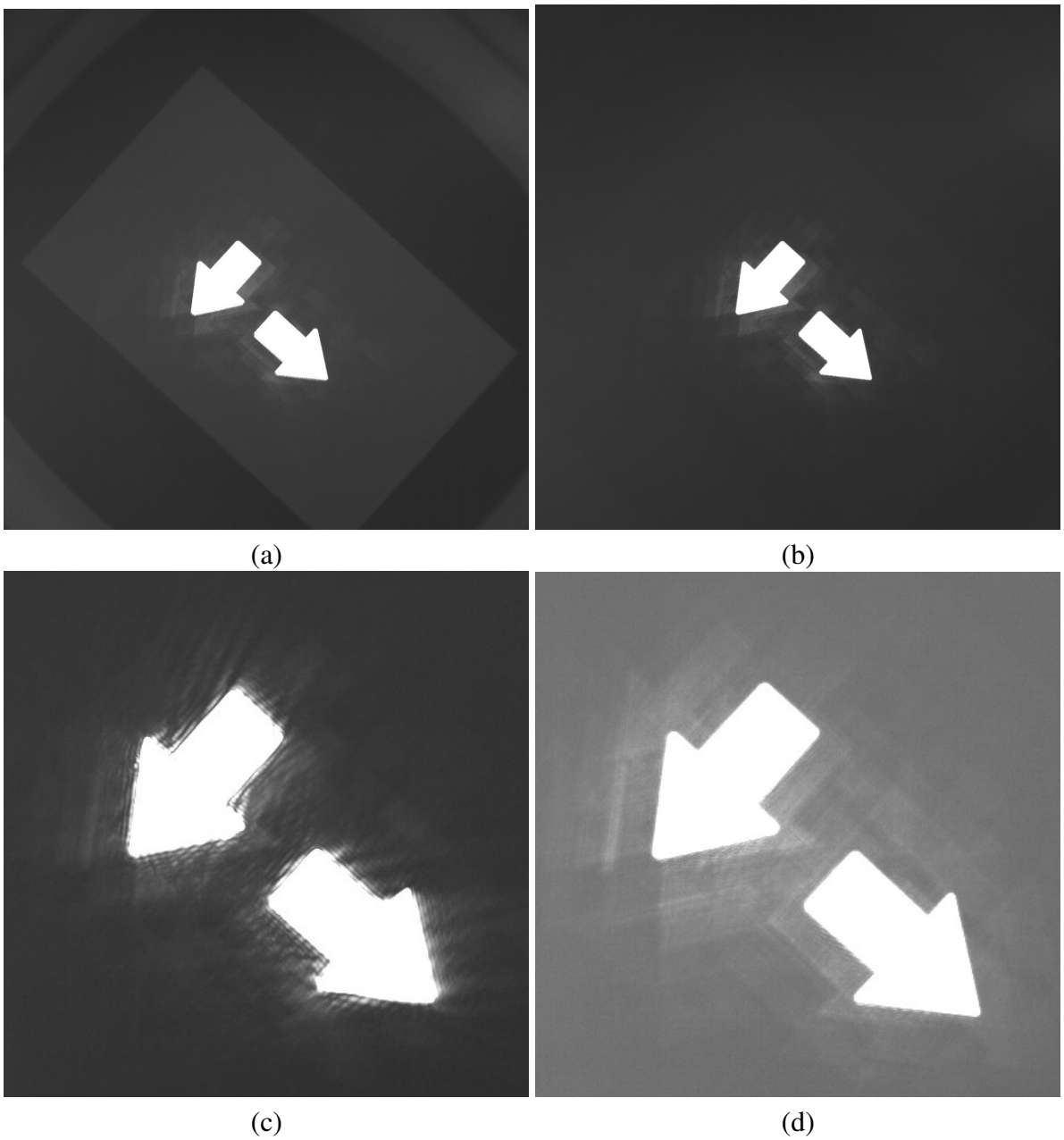

(a) (b)

(c) (d)

Figure 4.9 Pictures of the intermediate image plane, illustrating the influence of the iris opening. Open iris (a), almost closed iris (c) and intermediate setting (b). While for an open iris light scattered from the vicinity of the chip is imaged onto the camera, the almost closed setting results in visible diffraction effects. An intermediate setting (b) of $\approx 5\,\mathrm{mm}$ results in a good trade-off between both effects. For a better visibility of these features the images are overexposed. Ghost-like images of the original arrow pattern are visible in all images. Sub-figure (d) shows an image at the same setting as (b), but with even higher exposure time for a better visibility of those.

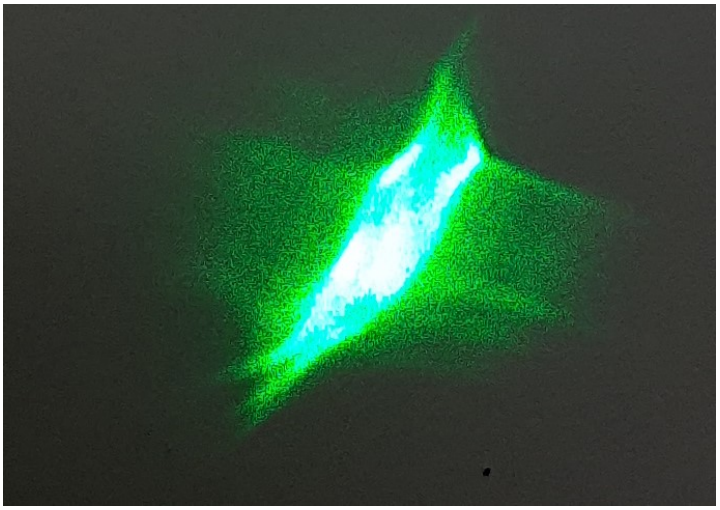

Figure 4.10 Distortions of the phase profile, introduced by an uneven plane of the chip, visible in a picture of the free space beam without any optics after the DMD and all mirrors in the same position. Although the beam is expected to have a Gaussian shape, this is not the case. The same pattern, but smaller, can be observed between the two 4f-systems.

applications of DMDs in phase space [22]. Whereas in those applications a phase map can be measured beforehand and then compensated, the real space setup does not have this option. While the consequences of this are also less severe in real space applications, this could be a source of uneven intensity distributions.

Evidence for this was found, by scrambling the phase of the illuminating laser. This was realized with a sheet of paper. Scattering on the paper is not sufficient to break the coherence, because the coherence length of the laser is much larger than the lengths scales involved in the scattering process. The result is a speckle pattern on the camera. However, for inducing vibrations of the paper, much faster than the exposure time of the camera, the interference effects average out. The resulting intensity distribution is much smoother than that of all tests performed with coherent light. Fig 4.11 shows an example of this for a stripe pattern displayed on the DMD next to one of the smoothest distributions, captured with coherent light, for comparison.

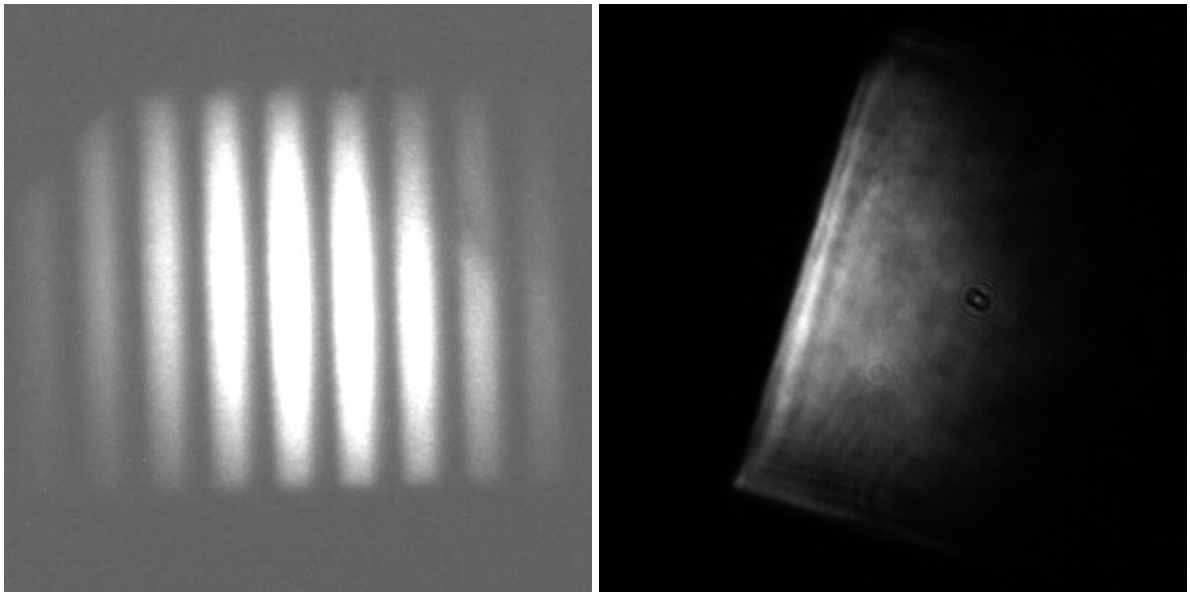

(a) (b)

Figure 4.11 Further investigation of the phase distortions by comparison of pictures of a stripe pattern taken with a phase scrambler technique (a) and a wall shape, dividing the chip into two halves, during illumination with coherent light (b). Disregarding the saturated regions in the center, (a) has a smoother intensity profile than (b). While the diffraction orders on the edge are expected, unevenness in the intensity can also be observed far off the wall.

5 Distortions and Compensation

Since distortions arise in the projection optics, one needs a way to quantify and ideally compensate those. Quantifying can be done by reimaging the atom plane onto a camera as before and comparing the result to the displayed pattern on the DMD. For this, one first needs a rough estimate of how the image transforms. In practice, this is done by first finding the center point of the DMD on the camera and then looking for orientation and demagnification. From there, one can either search for distortions of the relative positions of multiple spots in the image, and compensate for those, or try to optimize with random mirror flips, which should also be able to optimize for minimum higher orders like discussed in 3.2.2. The reimaging employs the same camera as used earlier. Instead of using the manufacturer's viewing software, an API wrapper called Pymba is employed. This was needed to automatize the optimization procedures within Python.

In the following two kinds of distortions on the image will be distinguished. First, the large scale distortions that make initially straight lines look curved, like the ones that appear when looking through curved glass. This also includes tilts of the whole picture, which was a problem reported by groups working with similar setups. Second, the small scale errors that arise from interference effects. This distinction is made because the means of quantifying and compensating those differ. While the reduction of diffraction effects was discussed earlier for an ideal field-PSF, the same principle also holds in the presence of aberrations that alter the shape of the point spread function.

5.1 Distortions on large Scales

The initial goal of the algorithm described in the following is to quantify large scale errors. Afterwards, those measurements are used to give the inverted errors on the input picture.

5.1.1 Quantifying Distortions

This algorithm works based on finding spots in the camera images and comparing their positions to the positions on the DMD, where the spots are generated by flipping a patch of 16 by 16 mirrors. Two-dimensional Gaussians are fitted to the spots to find those in the pictures. While a Gaussian only approximates the PSF of a spot, this procedure is computationally efficient, and only the centers of the spots are of interest for quantifying the spot position in form of a point. The algorithm to find distortions in the image works as follows:

1. Center point: A patch in the center of the DMD is turned on and found on the camera by fitting a Gaussian to the resulting image. This yields the origin of the camera's coordinate system.

2. Orientation and demagnification: Three patches arranged in an L-shape are turned on, and three Gaussians are fitted to the image. From there, the points are identified by their distances to the center, and a mean demagnification is inferred. Projection on their original coordinate vectors yields the orientation angles. Ambiguities of the angles (ϕ or $2\pi - \phi$) are resolved, and a check if the image is mirrored is performed. This is done by checking in which quadrants the points are found.

3. Errors over the DMD area: A sweep through the chip is performed by successively turning on patches on the chip together with the center patch for comparison. Again, the spots on the camera are fitted. The resulting points can then be transformed back into the chips frame with the information found in 2. The differences between the points and the original patch position on the DMD give the distortions of the projection optics (assuming a perfect imaging on the camera).

Fig. 5.1 shows the resulting points as well as the original positions on the DMD and Fig. 5.2 the corresponding pixel errors in the plane of the chip in x- and y-direction. The errors do follow some pattern, like the y-error increasing from the top left to bottom right. This variation, though, is on the order of $\approx 40\,\mathrm{px}$ over a distance of almost $2000\,\mathrm{px}$. Therefore, this does not indicate any major large scale distortions like tilts. This can be attributed to the chip alignment capabilities of the setup and the fact that the output optics is aligned with the normal vector of the plane of the chip in the first place.

Although the measured area is far from giving a complete picture over the whole chip, it includes the most relevant areas. The missing areas on the longer x-axis of the chip are not included in the potential shaping, also because they are not illuminated. Points in the vicinity of the center point are expected to have low errors, as this is the point of reference. The reason that the algorithm does not work in these areas is due to the underlying fitting procedure. Fitting multiple two-dimensional Gaussians into the same much larger image is computationally costly. A preceding function is, therefore, employed to assign pixels, brighter than a given threshold, to distinct clusters. Then the fitting procedure only has to account for pixels in those areas and, more importantly, only has to fit single Gaussians (multiple times). While the speedup is immense, the disadvantage is that the cluster assignment is more error-prone, if the spots are too close to each other.

To get a reference for the reliability of the errors found, one can take a look at the variances of the fit. Subsequently, those are compared to the deviations of the fitted center point positions, which are measured as a reference for every point in step 3. While both were small in absolute numbers, the fact that they differ substantially raises doubts on the precision of the errors found for the other points.

A Gaussian is a good approximation to the Airy disc, which was also reflected in small variances, reported by the fitting function. For the center point, corresponding standard deviations are on the order of $0.003\,\mathrm{px}$, which is negligible, even after transformation in the DMD frame (including the magnification found in step 2 of ≈ 7). A standard deviation of the center point position can also be inferred from the different measurements, which were carried out in step 3. The values found are on the order of $0.15\,\mathrm{px}$ in x- and $0.12\,\mathrm{px}$ in y-direction, which, after transformation into the DMD frame, is roughly a pixel. Although, this may include over time effects like drifts of the setup, the difference corresponds to a factor 50

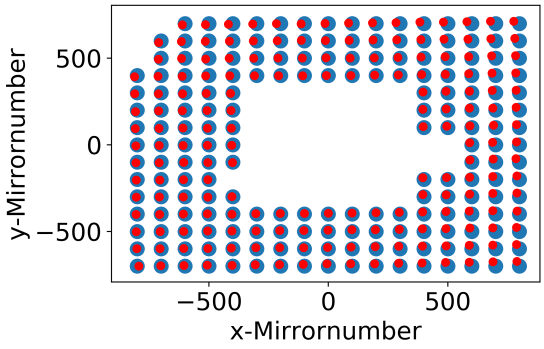

Figure 5.1 Points, measured by fitting to spots on the camera picture and transforming to the DMD's plane (red), and the original patch positions on the DMD (blue). Not the whole chip area of $2560 \times 1600\,\mathrm{px}^2$ was examined. For the outermost areas this is due to the low light intensity relative to the center. Close to the center the individual spots can not be separated by the algorithm (although they are resolvable). These effects also lead to failures in the algorithm where spots are missing, in addition.

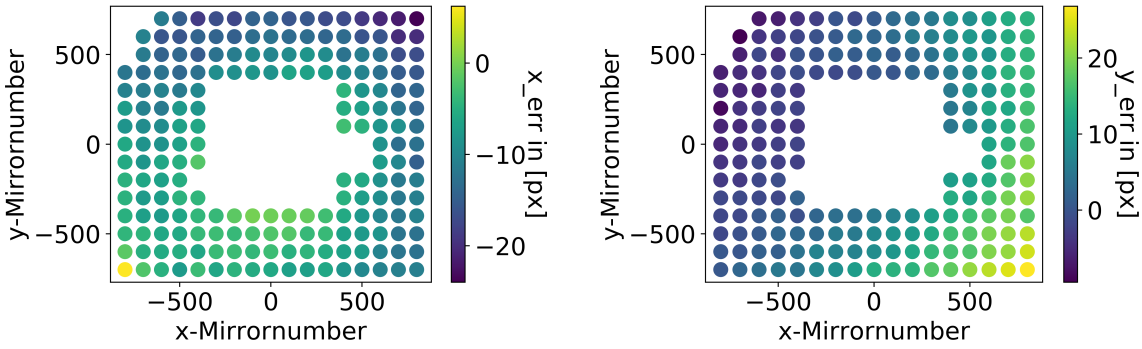

(a) (b)

Figure 5.2 Distortions measured, of Fig. 5.1, split in x- (a) and y-direction (b). The fact that all errors are smaller than $30\,\mathrm{px}$ rules out major distortions on the large scale.

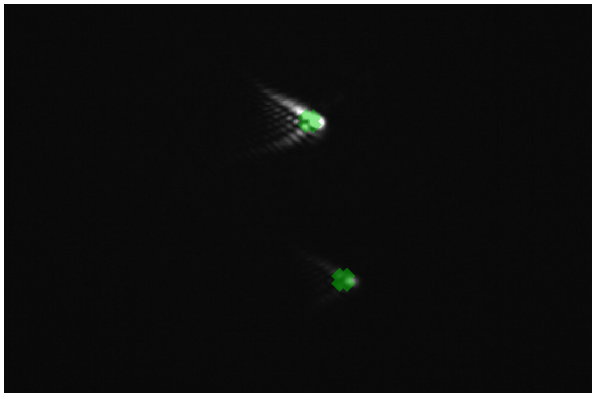

Figure 5.3 Fitted points (green) of two spots with the last $750\,\mathrm{mm}$ lens misaligned. One can see strong asymmetric higher orders of the spots (comatic aberration), which lead to the Gaussian fit being shifted away from the main order. Those errors lead in turn to errors in the estimation of the image distortion.

between the two errors. For points measured close to the center, the deviations of the fit differ only slightly from that of the center point. As one goes further out these deviations rise by more than one order of magnitude. Still, there are some outliers, for that the error is two magnitudes higher, and 4 points for which no variance was returned by the fitting function. To investigate this further, the last lens has been strongly dealigned. It became apparent that the fitted positions have systematic errors, in addition. This can be seen in Fig. 5.3 where the PSF suffers from a large comatic aberration. While this does not invalidate the conclusion that the large scale errors are small, it can impact the capabilities of the compensation algorithm presented subsequently.

5.1.2 Compensation on large Scales

In this section, an algorithm is presented that tries to compensate for the errors found before. It does so by first building up a transformation matrix M_{dist} from the errors, which transforms a pattern into its corresponding distorted form. In the next step, it is transposed. This way, it functions like a look-up table returning a mirror position to turn on, given light at a position is desired.

First, the errors for every mirror on the chip are inferred from the points measured. This is done by taking the mean over the ten nearest measured points, weighted by their distances. From there, the distorted position for each mirror is calculated by taking its position and adding the interpolated error. The resulting decimal position is then discretized by the overlap of a square with the four nearest mirror positions. Entering those four values into the corresponding positions of a $2560 \times 1600\,\mathrm{px}^2$ grid, then defines the distorted image of a single mirror. By now reshaping this image to a vector $\vec{x}_{dist}$, one can build up the transformation Matrix M_{dist} with columns consisting of those vectors, each corresponding to an input pixel. For an input picture $\vec{x}_{in}$, the distorted picture can, therefore, be calculated:

$$\vec{x}_{dist} = M_{dist} \times \vec{x}_{in} \tag{5.1}$$

Ideally, one would now want to invert (or at least pseudo-invert) this transformation. However, since the resulting matrix has 4096000 rows and columns ($\approx 16.8 \times 10^{12}$ entries, although most are zero), this is not feasible. Instead, the assumption $M_{dist}^{-1} = M_{dist}^{T}$ is made, which would be given, if it were not for the overlap between neighboring pixels, resulting from the discretization of the distorted positions, and edge pixels, that can be shifted in or out of the chip area. Without those two effects the matrix would consist of a full set of orthonormal basis vectors, and define a change of basis between the input and distorted frames. Nevertheless, treating the transposed matrix as being the inverse, in the case of the matrix calculated here, can be justified by looking at the resulting structure of $M_{dist}^{T} \times M_{dist}$ in Fig. 5.4. It is not far off an identity matrix with additional entries stemming from the overlap between neighboring pixels.

This can now be used to optimize arbitrary patterns by multiplying the desired pattern in its vector form with the transposed matrix. Because the resulting pattern is not binary, the FS-algorithm is employed to binarize again.

Fig. 5.5 shows an example of an optimized pattern (b), next to the inverted errors (a) found previously (which are the resulting shifts). Disregarding the edges where areas without image

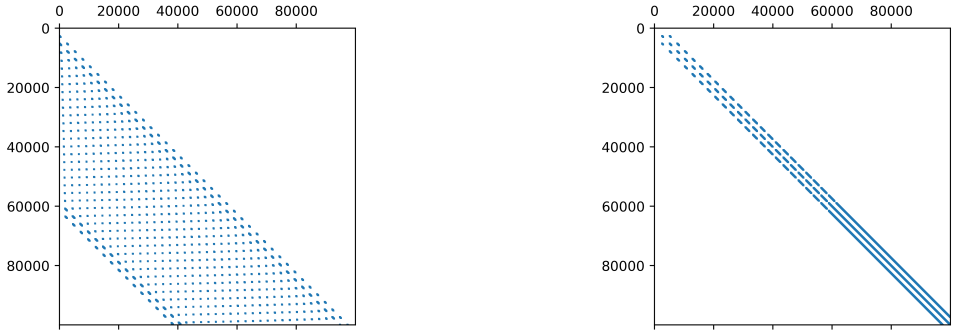

(a) (b)

Figure 5.4 Structure of the first 10^5 rows and columns of the transformation matrix M_{dist}, which transforms an image into its distorted form (a) and multiplied with itself transposed M_{dist}^T (b), which is expected to be a good estimate of its inverse. All non-zero entries are marked in blue. Despite for small indices where the errors shift positions out of the DMD area and therefore entries are missing, (b) consists of the diagonal plus overlap between neighbouring pixels only.

information shifted into the DMD area and vice versa, the corrections are hardly noticeable. A test where single patches were optimized and subsequently measured as described previously showed no significant improvements in the measured distortions. One explanation for this could be the uncertainty of the measured distortions themselves, combined with the fact that these are small. While the principle holds, if large scale distortions arise in the final setup (for example if the blaze condition needs to be fulfilled at some point), no major improvements for the patterns in the test setup are anticipated. Subsequently, an algorithm that focuses on small scale distortions is presented.

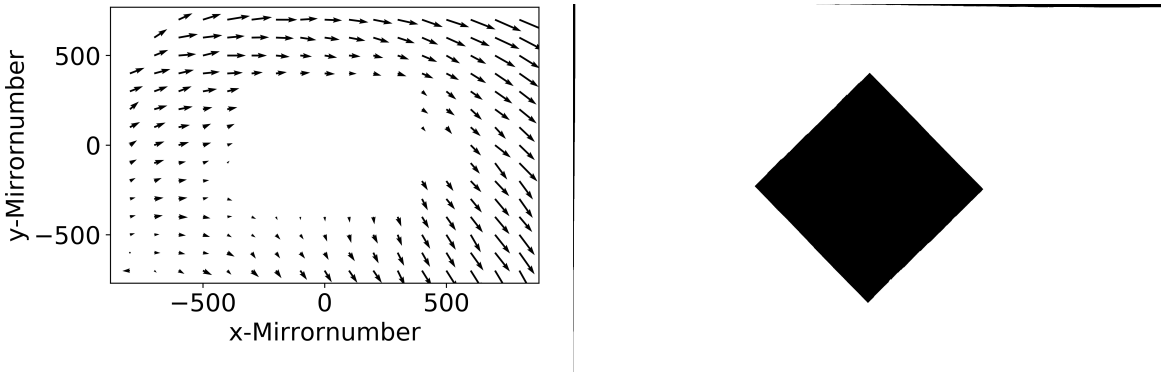

(a) (b)

Figure 5.5 Measured errors in form of resulting shifts (a) and compensated square pattern on the DMD (b). Note that the shifts in (a) have been enlarged by a factor 5 for better visibility. Differences in (b) are hardly visible. Most notably are the edges where areas without image data got shifted into the DMD area.

5.2 Compensation on small Scales

The algorithm to reduce distortions on small scales is inspired by Monte-Carlo methods and therefore combines quantifying and compensating distortions in a single algorithm. It first evaluates a cost function of a pattern reimaged on the camera based on differences to the desired ideal intensity distribution. Afterwards, the state of random mirrors is switched, and the cost is calculated again. If it went down, the intensity distribution got closer to the ideal one, and the changes are accepted. Otherwise, they get discarded. Over many iterations, the pattern is gradually optimized, ideally, up to the point where an acceptable cost value is reached. This can not be realized with the early implementation presented here.

The immediate downside of this approach is that every pattern needed for experiments has to be optimized individually. In return, a variety of different distorting effects can be tackled at once. As discussed in 3.2, one wants to get rid of higher orders of the PSF inside the black region. While this is the main reason for this approach, other effects like uneven intensities or even residual large scale errors can also be corrected. In principle, the whole pattern could even be built from scratch, starting with a blank DMD-chip.

To get started, a cost function must be defined first. For this, an ideal intensity pattern is designed in the DMD's frame. In addition to the dark and bright regions, a border area is defined. Then the cost is evaluated by adding measured intensities over the background for the dark region and intensities under a given threshold for the bright region. To allow for assignment of camera pixels to those regions, a center point and orientation are found, like in steps 1 and 2 of the previous section. With this, individual pixels can be transformed into the DMD's frame and evaluated. An additional safety factor in the cost evaluation is implemented to reduce the number of erroneously accepted switches. As it is not feasible to measure the influence of single mirror switches, many mirrors in an area (in the following called a patch) are switched at once. Because improvements, which exceed the safety factor are rare, multiple patches are modified simultaneously and their cost is evaluated individually.

In the following the different steps of the algorithm are described in more detail, a functional block diagram can be found in Fig. 5.6.

1. Orientation and background: To make evaluation of the cost possible, the algorithm first finds a center point on the camera as well as the orientation, like in steps 1 and 2 of the distortion algorithm in 5.1. An additional picture, without any mirrors turned on, is taken to estimate the background on the camera.

2. Evaluate cost function: First, a picture is taken. Every pixel of the area to optimize on the camera is transformed back to the DMD's frame and compared to the ideal image. The cost of each pixel gets evaluated by taking either the intensity needed to reach a given minimal power for the bright region or the intensity over the estimated background for the dark region:

$$c = \frac{\sum_{x_i} (I(x_i) - I_{bg}) + \sum_{x_{j'}} (I_{th} - I(x_{j'}))}{\sum_{x_i} + \sum_{x_j}}$$

   whereas x_i and x_j denote the pixels in the bright and dark areas, $x_{j'}$ only includes pixels under the minimum intensity threshold set. All Intensities are evaluated as 8-bit grayscales and take values between 0 and 255.

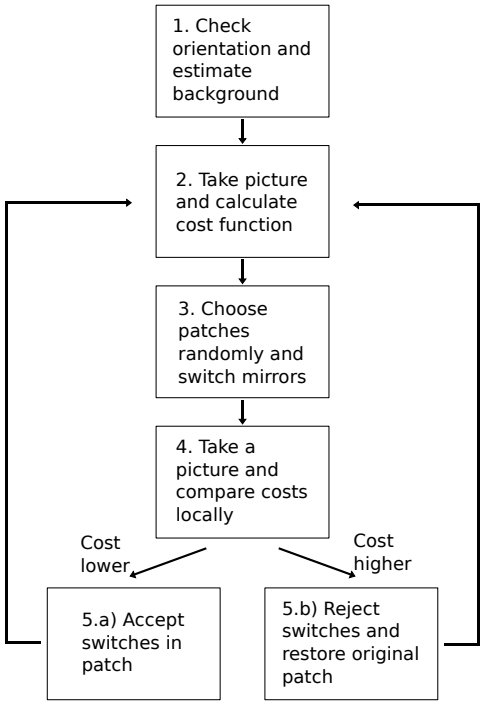

Figure 5.6 Block diagram illustrating the functionality of the algorithm used for compensation on small scales. A detailed description for every step can be found in the text.

3. Choose patches to optimize: A predefined number $N_{patches}$ of patches with a given size d^2 on the camera, are chosen. This is done randomly from the whole optimization area. The only additional constraint is that they are not close to each other. In each of the corresponding DMD patches N_{flip} mirrors are chosen randomly to switch their state.

4. Compare cost locally: Again, a picture is taken, and the cost is evaluated, like in step 2. But instead of taking the whole chip into account, the cost of each individual patch is calculated and compared to its value in the previous picture.

5. Accept or Restore: Every patch that lowered its cost after additional multiplication with a safety factor is accepted. All others are restored to their previous state. The resulting pattern is taken for the next iteration starting from 2.

In principle, this could be enough to optimize the pattern gradually. As a testing scenario, a straight wall shape was taken as the ideal distribution. The border region was initialized in a checkerboard fashion, to get a starting pattern on the DMD. This border region has a width of 6 mirrors and rules out ambiguities in the assignment procedure of camera pixels to a corresponding region, stemming from the pixel demagnification of 7. Nevertheless, since the patches on the DMD are much larger than that, those mirrors will still be switched. The algorithm was tested over 100 iterations, and an area of $50 \times 50\,\mathrm{px}$ on the camera to be optimized. The parameters have been set to $N_{patches} = 3$, $d = 7\,\mathrm{px}$, $N_{flip} = 360$ and a safety factor of 1%.

As one can see in the evolution of the total cost function (Fig. 5.7), the patterns got worse for a large number of steps. The main reasons for this are the facts that the background is only

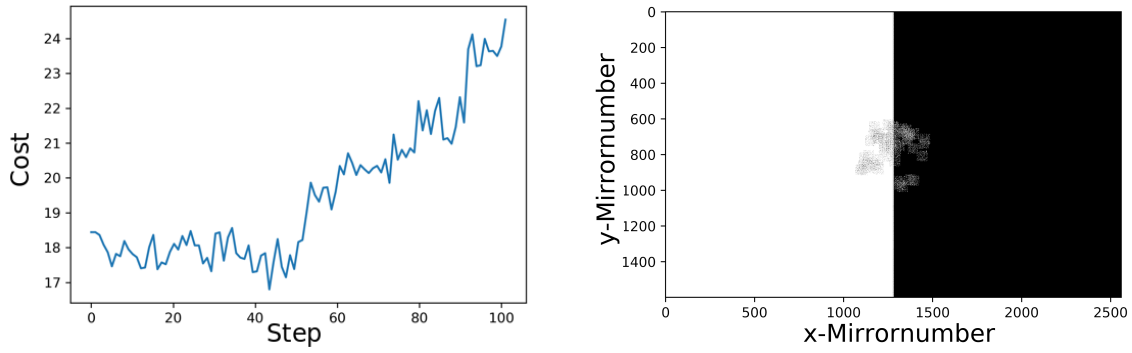

(a) (b)

Figure 5.7 Evolution of the cost function over 100 iterations (a) and and best configuration found for the DMD (b). While up to the 50^{th} iteration better or similar configurations are found, the cost makes a jump there and does not recover. Looking at (b) one can clearly make out the patches that have been altered. As some areas remain untouched, this is a clear sign that those few iterations are not sufficient. Although the altered region is small compared to the total chip size, it is much larger than what is expected to be relevant for the wall steepness, but corresponds to $50 \times 50\,\mathrm{px}$ on the camera only.

evaluated once, and the missing power stabilization, as it was not running during the test, but is crucial for shot-to-shot comparisons. If the cost of a patch went down because the background or power changed while optimizing, its new configuration is accepted. In future iterations, it is virtually impossible to fix those erroneous switches, since its unlikely that the same mirrors are chosen to switch back, as they are chosen randomly without consideration of the cost function. Raising the safety factor alone will not prevent this, since it also needs to be low enough that better configurations can be accepted. Restricting the area from which the patches are drawn to the bright region was tried. This did stop bright spots from appearing in the dark region, but not jumps in the cost function, as it does not address the underlying problem.

While it is needed to change many mirrors at once to get a measurable difference on the camera, one way to fix this would be to include the supposed influence on the cost function in the way the mirrors are chosen. For example, the probability for mirrors in the dark region and the ON-state to be chosen could rise as a function of the local cost and the distance to the wall. In addition, the power stabilization needs to be employed, and the background could be evaluated before every shot. All algorithms presented in this chapter would also benefit from a better resolution of the reimaged pattern. This could already be achieved by a higher magnification and, in turn, more efficient use of the area of the camera, which is also implementable in the final setup.

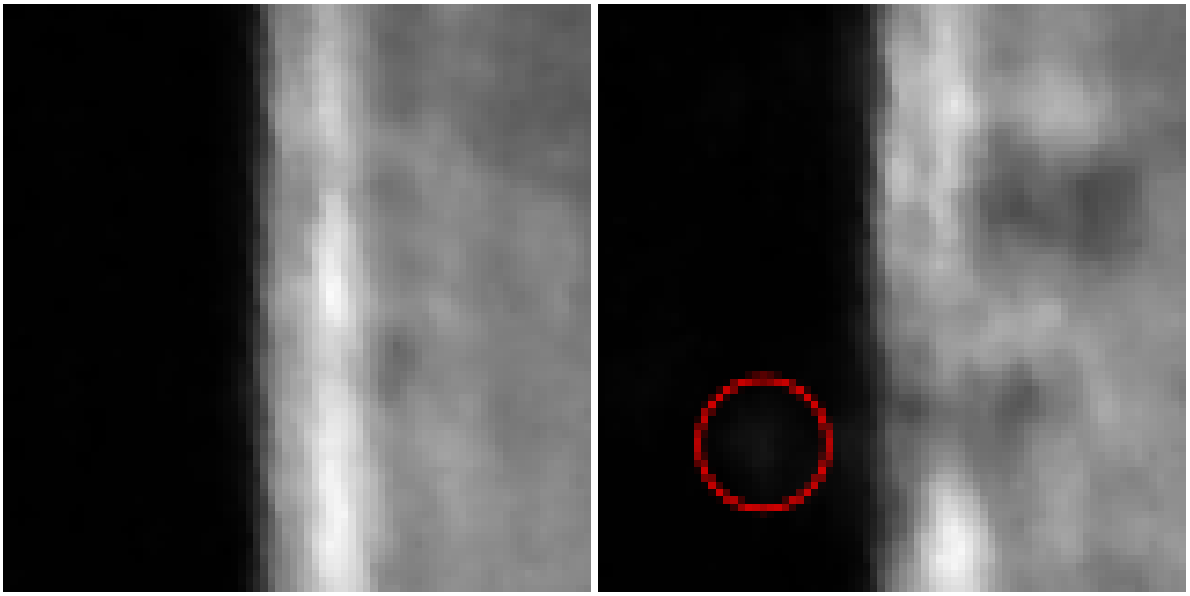

(a) (b)

Figure 5.8 Zoom-in on the initial camera picture (a) and after 42 iterations (b), which is the camera picture corresponding to the DMD pattern in Fig. 5.7. Although the cost function suggests that (b) shows the best pattern found, one can already see the effect of wrongly accepted patches. This is visible, in the dark region in form of brighter areas (red circle), or in the bright region in form of darker areas (e.g. top-right). Still the interference at the edge seems to be broken up for parts of the region.

6 Conclusion and Outlook

This thesis describes the design, building and testing of a setup that enables the generation of arbitrary two-dimensional optical potentials to trap neutral atoms. In essence, this is realized utilizing a Digital Micromirror Device to shape a laser beam to create the desired potential structure projected into the atom plane of the trap.

For the design, feasibility studies were carried out related to the basic criteria required to create arbitrary potentials, including the potential height, spatially variable intensity and mitigation of diffraction effects. Numerical calculations showed, that a potential height of $1\,\mathrm{k_B\mu K}$ is achievable, at $1\,\mathrm{W}$ laser power, which is well within the capabilities of the setup. The implementation of varying intensities (grayscales) turned out to be best realized via spatial averaging of the binary amplitude modulation provided by the DMD. The mitigation of diffraction effects at potential walls is achievable by choosing optimized wall patterns such that the higher orders interfere destructively.

A test setup was built and characterized, which can in large parts be transferred to the experiment. Additionally, two algorithms were designed and programmed, which are employed to measure and compensate distortions. The first algorithm is suitable for the correction of large scale distortions. In the test setup, it was possible to eliminate them by careful alignment of the DMD. The working principle of the second algorithm aims at the compensation of small scale distortions by automatically optimizing patterns, as is needed to mitigate diffraction effects near wall patterns. The algorithm shows first promising results, but further development is needed.

Further steps in the testing of the setup could include the use of the final objective. This may reveal distortions and problems that might appear in the final deployment in the experiment. Furthermore, the performance of the optimization algorithms may benefit from the higher resolution. The same holds true for the implementation and optimization of gray scales.

After these final tests, the setup can be included in the main experiment. Since a lattice potential for confinement in gravity direction is already installed, and imaging of the 2D geometry is possible, the main setup will then be ready for the first experiments.

A first research area is the simulation of the dynamics in the reheating process of the early universe after expansion. For this, a BEC is prepared in a flat box potential, and the interaction is modulated periodically in time by using a Feshbach resonance, which populates the low momenta via a parametric resonance. Together with the observation of the resulting long-term dynamics, this provides insight into the reheating process [23].

In addition to box-like potential walls, as used in the above experiment, the setup is suitable for creating arbitrary potential shapes. These can, for example, be used to generate not only trapping potentials but also prepare initial conditions with modulated density or phase distribution in the area occupied by the BEC, further increasing the parameter space for the preparation of ultra-cold atomic clouds.

Bibliography

[1] A. Ashkin. *Acceleration and Trapping of Particles by Radiation Pressure.* Phys. Rev. Lett. **24**, 156–159 (1970).

[2] A. Ashkin. *Optical trapping and manipulation of neutral particles using lasers.* Proceedings of the National Academy of Sciences **94**, 4853–4860 (1997).

[3] M. Anderson, J. Ensher, M. Matthews, C. Wieman, and E. Cornell. *Observation of Bose-Einstein Condensation in a Dilute Atomic Vapor.* Science **269**, 198–201 (1995).

[4] K. B. Davis, M.-O. Mewes, M. R. Andrews, N. J. van Druten, D. M. K. D. S. Durfee, and W. Ketterle. *Bose-Einstein Condensation in a Gas of Sodium Atoms.* Phys. Rev. Lett. **75**, 3969–3973 (1995).

[5] A. Einstein. *Quantentheorie des einatomigen idealen Gases.* Sitzungsberichte der Preussischen Akademie der Wissenschaften , 261–267 (1924).

[6] A. Einstein. *Quantentheorie des einatomigen idealen Gases: Zweite Abhandlung.* Sitzungsberichte der Preussischen Akademie der Wissenschaften , 3–14 (1925).

[7] C. D'Errico, M. Zaccanti, M. Fattori, G. Roati, M. Inguscio, G. Modugno, and A. Simoni. *Feshbach resonances in ultracold 39K.* New Journal of Physics **9**, 223 (2007).

[8] R. Grimm, M. Weidemüller, and Y. Ovchinnikov. *Optical Dipole Traps for Neutral Atoms.* Advances in Atomic, Molecular, and Optical Physics **42**, 95 (2000).

[9] T. Tiecke. *Feshbach resonances in ultracold mixtures of the fermionic quantum gases 6Li and 40K*. Ph.D. thesis. University of Amsterdam (2009).

[10] Y.-X. Ren, R.-D. Lu, and L. Gong. *Tailoring light with a digital micromirror device.* Annalen der Physik **527**, 447–470 (2015).

[11] D. Schäffner, T. Preuschoff, S. Ristok, L. Brozio, M. Schlosser, H. Giessen, and G. Birkl. *Arrays of individually controllable optical tweezers based on 3D-printed microlens arrays.* Opt. Express **28**, 8640–8645 (2020).

[12] B. L. Texas Instruments. *Introduction to ±12 Degree Orthogonal Digital Micromirror Devices (DMDs).* (2018).

[13] B. E. A. Saleh and M. C. Teich. *Fundamentals of Photonics* (John Wiley & Sons, Ltd, 2001) Chap. 2-4, pp. 41–156.

[14] C. J. Foot. *Atomphysik* (Oldenbourg-Verl., München, 2011) pp. XV, 428 S.

[15] G. Salomon, L. Fouché, P. Wang, A. Aspect, P. Bouyer, and T. Bourdel. *Gray-molasses cooling of 39 K to a high phase-space density.* Europhysics Letters **104**, 63002 (2013).

[16] J. L. Roberts, N. R. Claussen, S. L. Cornish, E. A. Donley, E. A. Cornell, and C. E. Wieman. *Controlled Collapse of a Bose-Einstein Condensate.* Phys. Rev. Lett. **86**, 4211–4214 (2001).

[17] P. Schuck and X. Viñas. *Thomas-Fermi approximation for Bose-Einstein condensates in traps.* Phys. Rev. A **61** (2000). 10.1103/PhysRevA.61.043603.

[18] S. M. Popoff and M. W. Matthès. *ALP4lib: A Python module to control Vialux DMDs.* (2016).

[19] G. Gauthier, I. Lenton, N. Parry, M. Baker, M. Davis, H. Rubinsztein-Dunlop, and T. Neely. *Configurable microscopic optical potentials for Bose-Einstein condensates using a digital-micromirror device.* Optica **10** (2016). 10.1364/OPTICA.3.001136.

[20] Microsoft. *Windows 7.* Sample Pictures.

[21] R. W. Floyd and L. Steinberg. *An Adaptive Algorithm for Spatial Greyscale.* Proceedings of the Society for Information Display **17**, 75–77 (1976).

[22] P. P. J. Zupancic. *Dynamic Holography and Beamshapingusing Digital Micromirror Devices*. Master's thesis. Ludwig-Maximilians-Universität München (2013).

[23] K. Geier, A. Chatrchyan, J. Berges, and P. Hauke. *unpuplished.* .

Danksagung

An dieser Stelle möchte ich allen danken, die mich während der vergangenen Jahr unterstützt, und damit zum Gelingen dieser Arbeit beigetragen haben.

- Zuerst möchte ich Prof. Markus Oberthaler danken, der diese Arbeit und die erneute Zeit am BECK erst ermöglicht hat, indem er mich wieder in seiner Gruppe aufgenommen hat. Er war immer optimistisch, was die Fortschritte am Experiment angeht, und ließ mir in der Umsetzung meines Aufbaus viele Freiheiten.
- Ebenso möchte ich Prof. Selim Jochim für die Übernahme der Aufgabe der Zweitkorrektur danken.
- Ganz besonders möchte ich mich auch beim gesamten BECK-Team bedanken. Bei Helmut Strobel, der mich immer wieder von seiner Expertise hat profitieren lassen, indem er mir bei allen möglichen Fragen und Problemen mit Rat und Tat zur Seite stand. Sowie Celia Viermann und Maurus Hans, die sehr viel Korrekturarbeit für diese Thesis geleistet, und bei der alltäglichen Arbeit im Labor immer wieder mit Diskussionen und Anregungen zum Gelingen beigetragen haben.
- Außerdem möchte ich mich bei der Werkstatt bedanken. Insbesondere bei David Jansen, der die Aluminiumhalterung gefertigt hat.
- Bei Prof. Jean Dalibard und seiner Gruppe am Kastler Brossel Laboratory in Paris möchte ich mich ebenfalls bedanken. Sie haben uns völlig uneigennützig zu sich eingeladen und uns an ihren Erfahrungen mit ähnlichen Aufbauten in ihren Laboren teilhaben lassen.
- Der gesamten Matterwave-Gruppe danke ich für die gute Zeit, das Frühstück am Freitag morgen, sowie eine Vielzahl kleinerer Hilfen und guter Gespräche.
- Zuletzt bedanke ich mich bei meinen Eltern, sowie meiner Freundin, die mich auch in dieser außergewöhnlichen Zeit unterstützt haben.

Erklärung

Ich versichere, dass ich diese Arbeit selbstständig verfasst und keine anderen als die angegebenen Quellen und Hilfsmittel benutzt habe.

Heidelberg, den 14.05.2020,